Naval Research Laboratory

Washington, DC 20375-5320

Quasi-Analytic Model of OTHR Clutter from Equatorial Bubbles in the Ionosphere

Paul A. Bernhardt

Charged Particle Physics Branch
Plasma Physics Division

February 27, 2006

REPORT DOCUMENTATION PAGE

Form Approved
OMB No. 0704-0188

Public reporting burden for this collection of information is estimated to average 1 hour per response, including the time for reviewing instructions, searching existing data sources, gathering and maintaining the data needed, and completing and reviewing this collection of information. Send comments regarding this burden estimate or any other aspect of this collection of information, including suggestions for reducing this burden to Department of Defense, Washington Headquarters Services, Directorate for Information Operations and Reports (0704-0188), 1215 Jefferson Davis Highway, Suite 1204, Arlington, VA 22202-4302. Respondents should be aware that notwithstanding any other provision of law, no person shall be subject to any penalty for failing to comply with a collection of information if it does not display a currently valid OMB control number. **PLEASE DO NOT RETURN YOUR FORM TO THE ABOVE ADDRESS.**

1. REPORT DATE *(DD-MM-YYYY)*	2. REPORT TYPE	3. DATES COVERED *(From - To)*
27-02-2006	Memorandum Report	

4. TITLE AND SUBTITLE

Quasi-Analytic Model of OTHR Clutter from Equatorial Bubbles in the Ionosphere

5a. CONTRACT NUMBER

5b. GRANT NUMBER

5c. PROGRAM ELEMENT NUMBER

6. AUTHOR(S)

Paul A. Bernhardt

5d. PROJECT NUMBER
67-8771-05

5e. TASK NUMBER

5f. WORK UNIT NUMBER

7. PERFORMING ORGANIZATION NAME(S) AND ADDRESS(ES)

Naval Research Laboratory, Code 6750
4555 Overlook Avenue, SW
Washington, DC 20375-5320

8. PERFORMING ORGANIZATION REPORT NUMBER

NRL/MR/6750--06-8911

9. SPONSORING / MONITORING AGENCY NAME(S) AND ADDRESS(ES)

Office of Naval Research
One Liberty Center
875 North Randolph Street
Arlington, VA 22203-1995

10. SPONSOR / MONITOR'S ACRONYM(S)

ONR

11. SPONSOR / MONITOR'S REPORT NUMBER(S)

12. DISTRIBUTION / AVAILABILITY STATEMENT

Approved for public release; distribution is unlimited.

13. SUPPLEMENTARY NOTES

14. ABSTRACT

Ground clutter for the over-the-horizon radar (OTHR) sky wave becomes Doppler shifted because the ionosphere through which the radio rays are propagating changes. One source of these changes is ionospheric bubbles, which rise vertically through a horizontally stratified plasma near the equator. The rising plume structures are formed when gravity, neutral winds, or external electric fields act on the F-region plasma. The effect of these ionospheric disturbances can be simulated by tracing rays through physics-based models of the equatorial bubbles. For the physics-based models, exact solutions for internal electric potentials are derived, assuming linear or circular symmetry to the density structures imbedded in the background plasma. A wide variety of analytic solutions for electric potentials are found for both density cavities and density enhancements. Quasi-analytic solutions for the transport of the bubbles are derived using the continuity equation for the plasma with production and loss terms neglected. The analytic models of the electric fields produce incompressible motion that transports the locations of "plasma cells" but do not change the density of the plasma in each cell. This Lagrangean approach employs a time-dependent, coordinate mapping of the undisturbed layer grid. Using internal electric potentials of the bubbles and external polarizations of the F-layer as a whole, a transport model yields tilted plasma plumes that move through the F-region. This time-dependent computer model provides useful plasma densities in a fraction of the time for fully numerical simulations. The electric potential derived in the models can be directly applied to the ray-trace computations to yield predictions for Doppler shifts in the unstable ionosphere.

15. SUBJECT TERMS

Over-the-horizon radar
Ionospheric irregularities
Computer model of the ionosphere

16. SECURITY CLASSIFICATION OF:			17. LIMITATION OF ABSTRACT	18. NUMBER OF PAGES	19a. NAME OF RESPONSIBLE PERSON
a. REPORT	**b. ABSTRACT**	**c. THIS PAGE**	UL	61	Paul Bernhardt
Unclassified	Unclassified	Unclassified			**19b. TELEPHONE NUMBER** *(include area code)* (202) 767-0196

Standard Form 298 (Rev. 8-98)
Prescribed by ANSI Std. Z39.18

CONTENTS

Quasi-Analytic Model of OTHR Clutter from Equatorial Bubbles in the Ionosphere

Paul A. Bernhardt
Plasma Physics Division
Naval Research Laboratory
Washington, DC 20375

Abstract

Ground clutter for the over-the-horizon radar (OTHR) sky wave becomes Doppler shifted because the ionosphere through which the radio rays are propagating changes. One source of these changes is ionospheric bubbles which rise vertically through a horizontally stratified plasma near the equator. The rising plume structures are formed when gravity, neutral winds or external electric fields act on the F-region plasma. The effect of these ionospheric disturbances can be simulated by tracing rays through physics based models of the equatorial bubbles. For the physics based models, exact solutions for internal electric potentials are derived assuming linear or circular symmetry to the density structures imbedded in the background plasma. A wide variety of analytic solutions for electric potentials are found for both density cavities and density enhancements. Quasi-analytic solutions for the transport of the bubbles are derived using the continuity equation for the plasma with production and loss terms neglected. The analytic models of the electric fields produce incompressible motion that transports the locations of "plasma cells" but do not change the density of the plasma in each cell. This Lagrangean approach employs a time dependent coordinate mapping of the undisturbed layer grid. Using internal electric potentials of the bubbles and external polarizations of the F-layer as a whole, a transport model yields tilted plasma plumes that move through the F-Region. This time-dependent computer model provides useful plasma densities in a fraction of the time for fully numerical simulations. The electric potential derived in the models can be directly applied to the ray trace computations to yield predictions for Doppler shifts in the unstable ionosphere.

I.   Introduction

High frequency (HF) over the horizon radar (OTHR) systems can track aircraft, missiles and ships for thousands of kilometers. These distances are achieved with sky-wave propagation that involves reflection and refraction in the earth's ionosphere. Under disturbed ionospheric conditions, the radar return spectra can be broadened by the motion of structures in the ionosphere where the radar path propagates. Radar signals that propagate near the equator can encounter plasma bubbles that are formed after sunset at the bottomside of the F-layer. When the ionosphere is no longer illuminated by the sun, ion-electron recombination causes the bottom of the F-region to become steeper. Simultaneous with this steepening, the layer is lived by electric fields driven by the dusk terminator neutral winds. This process causes the F-layer to become unstable as the Rayleigh-Taylor instability forms bubbles that form on the bottom and subsequently rise through the layer. The purpose of this report is to formulate a model of these bubbles and to use ray-trace techniques to determine the effects that equatorial structures with have on OTHR clutter.

OTHR clutter is primarily the result of backscatter from the ground that reflects the radar signal back to the source with a range delay. Motion of the ground reflection surface such as ocean waves can induce Doppler spread in the clutter signal. Even if the ground surface is fixed, spread clutter can be produced if the ionosphere changes in time along the radar path. The sources of short term ionospheric fluctuations that can produce Doppler spread in the radar clutter are (a) decay of the layer after sunset, (b) motion of the layer by tidal electric fields, (c) traveling ionospheric disturbances caused by acoustic gravity waves propagating in the neutral atmosphere, and (d) plasma instabilities that cause large scale irregularities in the plasma. The equatorial bubble is the most import irregularity that produces clutter at low latitudes. The ionospheric bubble OTHR clutter study proceeds in two phases. First a quasi-analytic model of equatorial bubbles is generated that (1) replicates all the features of naturally occurring ionospheric density structures and (2) can be used to calculate radar paths using ray tracing through the electron densities. Rays will be traced from a ground transmitter site through this model ionosphere to eventually arrive at on the ground for backscatter along the same path to the transmission point. Each ray is characterized by phase and ground path lengths. Temporal changes in the phase path produce Doppler shifts in the return echo. The group path gives the round trip time delay that will be assigned to a range bin. The frequency shift in each range bin is determined from the time rate of change of the phase path along the ray.

II. Overview of Ionospheric Bubble Models

The F-Region ionosphere can become unstable if a density perturbation becomes electrically polarized by external forces from electric fields, neutral winds, and gravitational acceleration. Near the geomagnetic equator, gravity can act on the plasma attached to the nearly horizontal magnetic field lines to produce unstable conditions. After sunset when the layer is lifted by ambient electric fields, the bottom-side steepens and plasma bubbles are formed. These bubbles rise through the layer in response to a Rayleigh-Taylor type instability. Also, winds or electric fields induce electric fields in both density cavities and enhancements that cause distortions in the density structures. These distorted plasma structures are responsible for distortion of radio propagation which lead to navigation errors and outages, communications systems failures, radar clutter, and degradation of surveillance systems. The modeling of ionospheric bubbles or density enhancements uses computer simulations the calculate the effects of self generated electric fields (E) that are driven by gravity, neutral winds and external electric fields. The equations for these simulations can be solved numerically using (1) flux corrected transport algorithms for transport of plasma and (2) direct or iterative solvers of the non-separable potential equations that describe the self-generated electric fields. The computational time for solving for the disturbed ionosphere is often prohibitive so analytic solutions to both the transport and potential equations are useful. Exact analytic solutions can be used for (1) testing of the numerical algorithms to determine errors produced by boundary conditions and numerical round-off and (2) time-dependent simulations of typical electron densities used for testing tomographic reconstructions of the disturbed F-layer and for tracing of radio ray paths through the region. The analytic solutions also yield insight into the conditions for production of ionospheric bubbles.

The computational and analytical techniques for simulations of equatorial bubbles are compared in Figure 1. Usually numerical models proceed as illustrated by the block diagram given in Figure 1a. A stratified model of the F-layer is perturbed by a small density disturbance. Gravity is allowed to setup an electric potential in this plasma. The electric potential is obtained with a numerical solution of a non-separable elliptic equation using a direct solver such as described in Appendix A. Once the electric potential is obtained, the plasma is transported in response to the electric fields for a small time step. A non-dissipative flux corrected transport algorithm (Zalesak, Ossakow and Chaturvedi, 1982) is then used to incrementally move the plasma disturbance. The process is repeated with the generation of a revised electric potential followed by more incremental plasma transport. All of these processes are numerically intensive and can require several hours of computation.
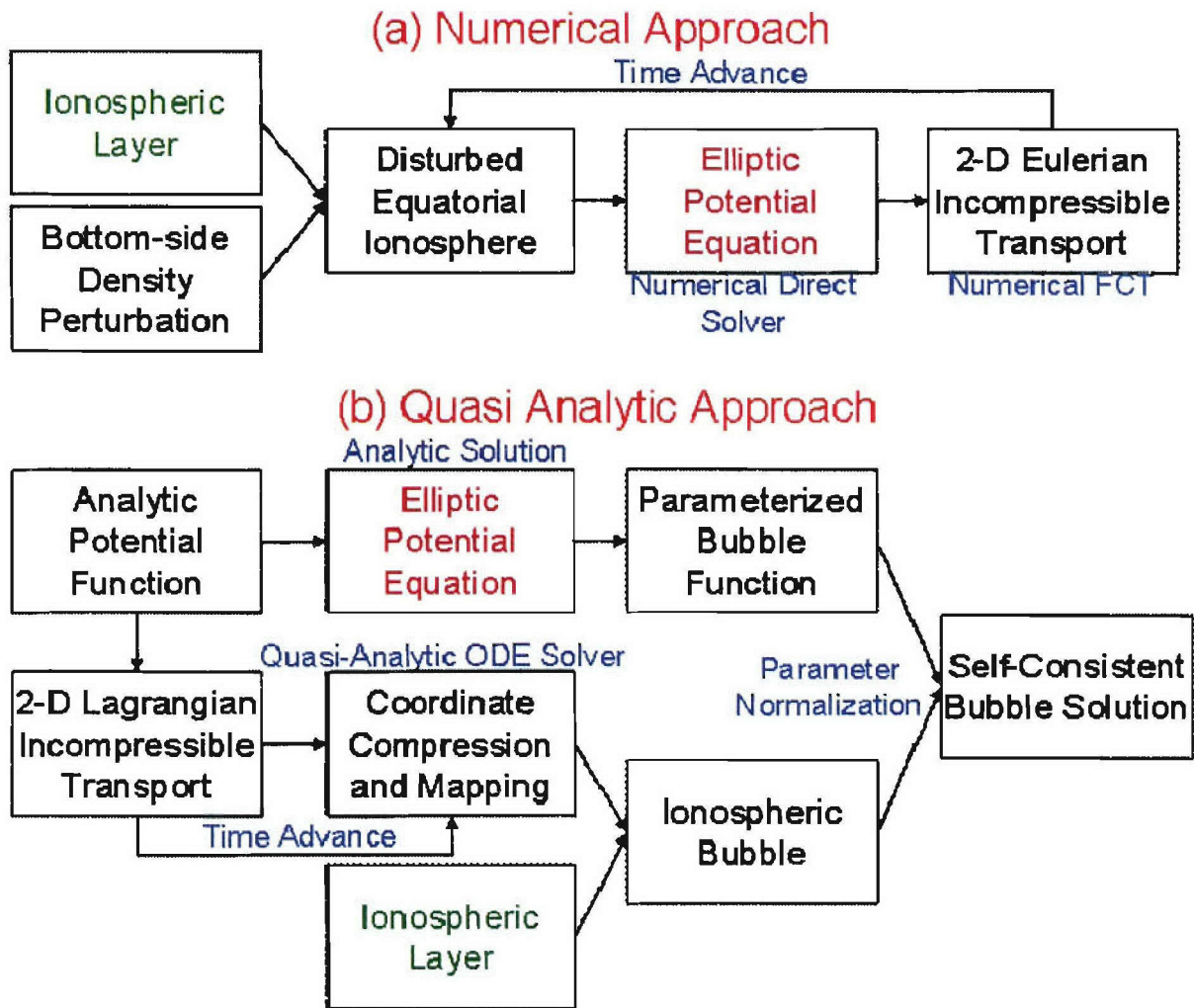

Figure 1. Block diagram of (a) numerical and (b) quasi-analytic algorithms for ionospheric bubble modeling. Both approaches use an equivalent set of equations but apply different solution techniques and different frames of reference.

The quasi-analytic model for the equatorial bubble is derived using the three steps in Figure 1b. This model is computationally faster than the fully numerical model and is more suitable for raytrace analysis. The components of the model are described separately. First the electric potential is defined by an analytic function and self-consistent expressions for electron density (or Pedersen conductivity) structures are obtained in the presence of electric fields, neutral winds and gravity. Second, the plasma transport is determined using incompressible motion from the induced electric fields. The plasma transport is derived with the analytic electric potential distorting the coordinates without changing the density in each coordinate cell. To realistically model ionospheric bubbles, the effects of neutral winds as well as gravity must be included. The polarization of the layer by a neutral tilts the ionospheric plume from the vertical. The third step is to adjust the parameters in the analytic models until the analytic solution given in step 1 matches the quasi-analytic results from step 2. The details of the electric potential and the plasma transport processes are described Sections III and IV, respectively. Introducing tilts and bifurcations in the model bubbles is described in Section V and, finally, Section VI describes normalization of the model to yield realistic time and spatial scales. Finally in Section VII, the propagation theory for determining Doppler shifts from ionospheric motion is described. A simple example for the velocity shifts from a rising ionosphere is used to test the model. Future work will use the computer models derived here to simulate the spread of the OTH radar clutter signals by both vertical and horizontal motion of bubbles in the equatorial ionosphere.

III. Analytic Models for the Electric Potential in a Disturbed Ionosphere

The equatorial ionosphere is commonly thought of as a uniform layer with the occasional imbedded structure or bubble. The modeling of ionospheric bubbles uses computer simulations that calculate the effects of self generated electric fields ($\mathbf{E}$) that are driven by gravity, neutral winds and external electric fields. The equations for these simulations can be found in a number of papers including Bernhardt [1988]. For the analytic solutions considered here, the background ionosphere will be uniform in the horizontal, x- and z-directions. The ambient magnetic field, $\mathbf{B}$, is aligned with the z-axis. The altitude variations of the undisturbed ionosphere will be represented by the function $n_{e0}(y)$ where y is the vertical coordinate.

The layer becomes distorted when a small perturbation grows as electric fields provide incompressible perpendicular motion at F-region altitudes. These internal electric fields move plasma across magnetic field lines with the velocity

$$\mathbf{v} = \frac{\mathbf{E} \times \mathbf{B}}{B_0^2} = -\frac{\nabla \Phi \times \mathbf{B}}{B_0^2} \tag{1}$$

where $\mathbf{v}$ is the velocity perpendicular to the ambient magnetic field $\mathbf{B}$ and the electric field $\mathbf{E} = -\nabla \Phi$ can be represented as the gradient of a scalar electrostatic potential Φ. Other perpendicular components of velocity driven by pressure gradients, neutral winds, and gravity can be neglected because the plasma in the F-region ionosphere is magnetized. This means that the electron and ion gyro frequencies are much larger than the corresponding collision frequencies with the background neutral gas.

4

An analytic approach is derived to solve for the electric potential for localized electron density perturbations driven by external vector fields. Kelley [1989] gives the electric current in the F-region as

$$\mathbf{J} = [\mathbf{E} + \mathbf{E}_0 + (\mathbf{U} + \frac{\mathbf{g}}{\nu_{in}}) \times \mathbf{B}] \sigma_P \qquad (2)$$

where $\sigma_p = \frac{e}{B_0} \frac{n_e \nu_{in}}{\Omega_i}$ is the Pedersen conductivity, $n_e(x, y, z)$ is the electron density, ν_{in} is the ion neutral collisions frequency, $\mathbf{E}_0$ is the external electric field perpendicular to $\mathbf{B}$, $\mathbf{U} = U_x \breve{x} + U_y \breve{y}$ gives the normal components of the neutral wind vector, $\mathbf{g} = -g_0 \breve{y}$ is the gravitational acceleration, and $\mathbf{B} = B_0 \breve{z}$ is the magnetic field vector. Assume that the normal electric fields are constant along the magnetic field in the z-direction and that there is no z-component of current $\mathbf{J}$. For specific gravitational accelerations, neutral winds and external electric fields, the potential equation is found from (2) using

$$\frac{\partial J_z}{\partial z} + \nabla_\perp \cdot \mathbf{J} = 0 \qquad (3)$$

Substitution of (2) into (3) and integration along the z-direction leaves an equation for the potential in the perpendicular ($\perp$) x- and y- directions.

$$\nabla_\perp \cdot (\Sigma_p \nabla_\perp \Phi) = \Sigma_p \nabla_\perp^2 \Phi + \nabla_\perp \Phi \cdot \nabla_\perp \Sigma_p = \nabla_\perp \cdot \int [\mathbf{E}_0 + (\mathbf{U} + \frac{\mathbf{g}}{\nu_{in}}) \times \mathbf{B}] \sigma_p dz \qquad (4)$$

where $\Sigma_p = \int \sigma_p dz$ is the field-line-integrated Pedersen conductivity and $\mathbf{E} = -\nabla_\perp \Phi$ is the induced electric field. For simplicity, the driving fields $\mathbf{E}_0, \mathbf{U},$ and $\frac{\mathbf{g}}{\nu_{in}}$ are assumed constant in space and time, then the potential equation simplifies to

$$\nabla_\perp^2 \Phi = \{[\mathbf{E}_0 + (\mathbf{U} + \frac{\mathbf{g}}{\nu_{in}}) \times \mathbf{B}] - \nabla_\perp \Phi\} \cdot \nabla_\perp \ln(\Sigma_p) = \{\mathbf{E}_T - \nabla_\perp \Phi\} \cdot \nabla_\perp \ln(\Sigma_p) \qquad (5)$$

where the equivalent electric field vector defined by $\mathbf{E}_T \equiv \mathbf{E}_0 + (\mathbf{U} + \frac{\mathbf{g}}{\nu_{in}}) \times \mathbf{B}$. Given a spatial distribution for the Pedersen conductivity (or electron density), the potential is usually obtained numerically from the non-separable elliptic equation (5). Often iterative solvers requiring relatively long solution times or direct solvers requiring large memories are required to compute this solution.

A computational alternate approach assumes that the potential is given and (5) is used to find the associated electron density. For this solution, only Pedersen currents in the horizontal, x-direction will be considered so

5

$$[E_{0x} + (U_y - \frac{g_0}{\nu_{in}})B_0]\breve{x} \equiv E_{Tx}\breve{x}$$
(6)

where E_{Tx} represents the equivalent driving fields from a static electric field in the positive x-direction, a neutral wind in the positive y-direction and gravitational acceleration along the positive y-axis. The sign of E_{Tx} is negative for the downward acceleration of gravity. In our notation, the growth rate for the Rayleigh-Taylor instability is $\gamma = (-E_{Tx}/B_0)/L_N$ where L_N is the scale length of the gradient on the bottom side of the ionosphere [Zalesak, Ossakow, and Chaturvedi, 1982; Sultan, 1996].

In normalized Cartesian coordinates, (4) becomes

$$\frac{\partial^2\hat{\Phi}}{\partial\hat{x}^2} + \frac{\partial Log(\Sigma_p)}{\partial\hat{x}}\frac{\partial\hat{\Phi}}{\partial\hat{x}} + \frac{\partial^2\hat{\Phi}}{\partial\hat{y}^2} + \frac{\partial Log(\Sigma_p)}{\partial\hat{y}}\frac{\partial\hat{\Phi}}{\partial\hat{y}} - \frac{\partial Log(\Sigma_p)}{\partial\hat{x}} = 0$$
(7)

where often gravitational forcing is the sole contribution to E_{Tx}, $\hat{\Phi} = \dfrac{\Phi}{E_{Tx}\,r_0}$ is the dimensionless, normalized potential, $(\hat{x},\hat{y}) = \left(\dfrac{x}{r_0}, \dfrac{y}{r_0}\right)$ are the normalized coordinates, and r_0 is a constant scale factor for all distances. Note that (7) has many self-similar elements. Multiplying the $\hat{x}$- and $\hat{y}$- coordinates as well as $\hat{\Phi}$ by a constant scale factor (i.e., r_0) does not change the equation. Multiplying Σ_p by a constant C_0 also yields a solution. Consequently, if $\hat{\Phi}(\hat{x},\hat{y})$ and $\Gamma_p(\hat{x},\hat{y})$ satisfies (7) then so do the pairs of functions $r_0\,\hat{\Phi}(\dfrac{x}{r_0}, \dfrac{y}{r_0})$ and $C_0\,\Gamma_p(\dfrac{x}{r_0}, \dfrac{y}{r_0})$. Normalized coordinates ($\hat{x}$, $\hat{y}$) will be used to simplify the notation for the analytic solutions.

The existence of analytic solutions for (7) was discovered by examining numerical solutions. A numerical algorithm for non-separable elliptic equations similar to (7) was written using a block tri-diagonal solver of the algebraic equation derived from finite difference approximations to the partial derivatives (Appendix A). When a circularly symmetric function, $\Sigma_p(\hat{r})$ where $\hat{r} = \sqrt{\hat{x}^2 + \hat{y}^2}$, was used for the Pedersen conductivity it was found that the integral of the resulting electric potential along $\hat{x}$ was also circularly symmetric. In mathematical terms,

$$\Sigma_p(\hat{r}) \Rightarrow \int\Phi(\hat{x},\hat{y})\,d\hat{x} = F_1(\hat{r})$$
(8)

This immediately shows that the form of the potential is the $\hat{x}$ coordinate multiplied by a circularly symmetric function since

6

$$\Phi(\hat{x}, \hat{y}) = \frac{F_1(\hat{r})}{\partial \hat{x}} = \frac{F_1(\hat{r})}{\partial \hat{r}} \frac{\partial \hat{r}}{\partial \hat{x}} = \frac{F_1(\hat{r})}{\partial \hat{r}} \frac{\hat{x}}{\hat{r}} = F_2(\hat{r}) \hat{x} \tag{9}$$

Functions of single variables such as $\hat{r}$ can be solved analytically.

General analytic solutions to (7) can be derived by making simplifying assumptions about the form of $\hat{\Phi}$ and $Log(\Sigma_p)$. Numerical simulations for symmetric perturbations in x with x-directed fields given by (6) yield electric potentials that are odd functions of x with the form

$$\hat{\Phi}(\hat{x}, \hat{y}) = (a_0 + a_1 \hat{x}) G[q(\hat{x}, \hat{y})] \tag{10}$$

where a_0 and a_1 are constants, $q(\hat{x}, \hat{y}) = \sqrt{\hat{x}^2 + s \hat{y}^2}$ is a single variable representing an elliptical perturbation for the potential and "s" determines the polarization of the coordinate ellipse.

The Pedersen conductivity (or electron density) takes the form of an elliptically shaped perturbation modulating the background conductivity.

$$Log[\Sigma_p^{(s)}(\hat{x}, \hat{y})] = L_p[q(\hat{x}, \hat{y}), s] + log[\Sigma_{p0}(\hat{y})] \tag{11}$$

where $L_p(q,s)$ is the natural log of the conductivity/density perturbation and $\Sigma_{p0}(\hat{y}) = \int \frac{e}{B} \frac{n_{e0}(\hat{y}, \hat{z}) v_{in}}{\Omega_i} r_0 \, d\hat{z}$ is the integrated conductivity associated with the horizontally stratified plasma layer. The last term of the left side of (7) is x-direction gradient of the log-Pedersen conductivity which drives the solution for the potential. Consequently, the $\hat{x}$ variation through the function q is required to obtain useful solutions for the potential.

Substitution of (10) and (11) into (7) and solving for the derivative of $L_p(q)$ yields the equation

$$L_p'(q,s) = - \frac{q^2 G'(q)\{\frac{2a_1 \hat{x}}{a_0 + a_1 \hat{x}} + s + s\hat{y}\frac{\partial log[\Sigma_{p0}(\hat{y})]}{\partial \hat{y}}\} + q^3 G''(q) + \hat{y}^2(s-1)s[qG''(q) - G'(q)]}{\frac{\hat{x} q^2[a_1 G(q) - 1]}{a_0 + a_1 \hat{x}} + q^3 G'(q) + \hat{y}^2(s-1)sqG'(q)]} \tag{12}$$

where the prime ($'$) denotes the derivative with respect to q. If the functions of $\hat{y}$ vanish, (12) may be integrated directly. The $\hat{y}^2$ terms vanish only if s = 0, or 1.

7

General solutions for an extended vertical plume imposed on a horizontally stratified ionosphere are considered first. For $s = 0$ the potential has no variations in the altitude coordinate ($\hat{y}$) and the solutions for (10) and (11) are given by

$$q = |\hat{x}|$$

$$\hat{\Phi}^{(0)}(\hat{x}, \hat{y}) = (a_0 + a_1 \hat{x})\, G(q)$$

$$L'_p(q, 0) = -\frac{2 a_1\, \hat{x}\, G'(q) + q\,(a_0 + a_1\hat{x})\, G''(q)}{\hat{x}\,[\,a_1\, G(q) - 1\,] + q\,(a_0 + a_1\hat{x})\, G'(q)} \tag{13}$$

$$\Sigma_p^{(0)}(\hat{x}, \hat{y}) = C_0 \Sigma_{p0}(\hat{y})\, \exp\!\left[-\int \frac{2 a_1\, \hat{x}\, G'(q) + q\,(a_0 + a_1\hat{x})\, G''(q)}{\hat{x}\,[a_1\, G(q) - 1] + q\,(a_0 + a_1\hat{x})\, G'(q)}\, dq \right]$$

where C_0 is a constant chosen to give the background conductivity as $\hat{x} \to \infty$. Exact solutions for pairs of Pedersen conductivity and electric potentials from (13) are easily found. Table I gives several examples these pairs.

Table I. Electron Density Disturbances and Companion 1-D Potential Functions

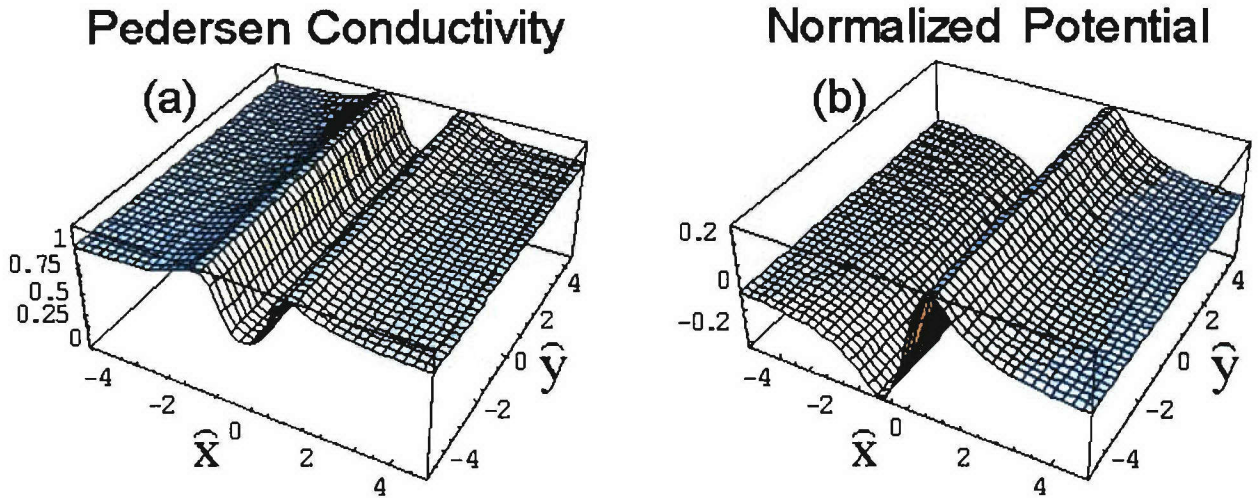| Pedersen Conductivity Function, $\Sigma_p^{(0)}(\hat{x}, \hat{y})$	Electric Potential, $\hat{\Phi}(\hat{x}, \hat{y})$
$\dfrac{\Sigma_{p0}(\hat{y})\, \exp(b\, \hat{x}^2)}{\exp(b\, \hat{x}^2) + 2\, b\,(a_0 + a_1\, \hat{x})\, \hat{x} - a_1}$	$(a_0 + a_1\, \hat{x})\, \exp(-b\, \hat{x}^2)$
$\dfrac{\Sigma_{p0}(\hat{y})\,(1 + |\hat{x}|^b)^2}{(1 + |\hat{x}|^b)^2 + a_1(b-1)\,|\hat{x}|^b - a_1}$	$\dfrac{a_1\, \hat{x}}{1 + |\hat{x}|^b}$
$\dfrac{\Sigma_{p0}(\hat{y})\, 2\cosh[b\, \hat{x}]^2}{1 - 2a_1\cosh[b\, \hat{x}] + \cosh[2\, b\, \hat{x}] + 2\, b\,(a_0 + a_1\hat{x})\sinh[b\, \hat{x}]}$	$(a_0 + a_1\hat{x})\, \mathrm{sech}[b\, \hat{x}]$

Figure 2. One-Dimensional Pedersen conductivity associated with the 1-D analytic electric potential using the parameters $a_1 = -0.5$ and $b = 3$. The topology of the solution remains unaffected by the choice of model parameters.

An example of the second function in Table I is illustrated in Figure 2 with the parameters a_1 = -0.5 and b = 3. The conductivity trough (Figure 2a) centered along the y-axis has a ridges that increase in amplitude as the parameter "a_1" is increased. If $a_1 > 0$, the trough is replaced by a Pedersen conductivity enhancement as the sense of the potential (Figure 2b) is reversed. The parameter "b" simultaneously controls the steepness of the walls on the conductivity irregularity and the spatial decay of the potential function. With separation of variables, even more general solutions to (7) can be found in Cartesian coordinates (Appendix B).

General Solutions for Circular Holes in an Ionosphere with simple vertical structure is considered next. For s =1 the density disturbance is circularly symmetric with radius r around the ($\hat{x}$, $\hat{y}$) origin. The solutions from (12) require $a_0 = 0$ and $a_1 = 1$ with the result

$$\hat{r} = \sqrt{\hat{x}^2 + \hat{y}^2}$$

$$\hat{\Phi}^{(1)}(\hat{x},\hat{y}) = \hat{x}\, G[\hat{r}] \tag{14}$$

$$L_p'(\hat{r},1) = -\frac{\{3+\hat{y}\,\dfrac{\partial \log[\Sigma_{p0}(\hat{y})]}{\partial \hat{y}}\}G'(\hat{r})+\hat{r}\,G''(\hat{r})}{G(\hat{r})+\hat{r}\,G'(\hat{r})-1}$$

To eliminate any dependence on of $\hat{y}$ in (14), the background Pederson conductivity takes the functional form

$\Sigma_{p0}(\hat{y}) = C_0\hat{y}^m$ where m and C_0 are a constants. With this substitution, (14) becomes

$$L_p'(\hat{r},1) = -\frac{(3+m)G'(\hat{r})+\hat{r}\,G''(\hat{r})}{G(\hat{r})+\hat{r}\,G'(\hat{r})-1} \tag{15}$$

which is identical to (13) with $a_0 = 0$, $a_1 = 1$ and m = -1. The corresponding formula for the spatial variation of Pedersen conductivity is

$$\Sigma_p^{(1)}(\hat{x},\hat{y}) = C_0\,\hat{y}^m\,\exp\left[-\int\frac{(3+m)\,G'(\hat{r})+\hat{r}\,G''(\hat{r})}{G(\hat{r})+\hat{r}\,G'(\hat{r})-1}d\hat{r}\right] \tag{16}$$

In Appendix C using separation of variables, all of the solutions for (7) in cylindrical geometry are derived.

The one-dimensional (s=0) and two-dimensional, circularly-symmetric (s=1) expressions are similar. With $a_0 = 0$ and $a_1 = 1$, the rational polynomial function of the form $G(q) = \dfrac{a}{1+q^b}$ used in (10), and the corresponding potentials from (13) and (14) are

$$\hat{\Phi}^{(0)}(\hat{x}) = \frac{\hat{x}\, a}{1+|\hat{x}|^b} \tag{17a}$$

and $\hat{\Phi}^{(1)}(\hat{x},\hat{y}) = \dfrac{\hat{x}\, a}{1+(\hat{x}^2+\hat{y}^2)^{b/2}}$ \hfill (17b)

where a and b are constants. Analytic solutions can be obtained from (13) through (16).

Derivatives of the density perturbations become

$$L'(q,0) = \frac{a\, b\, q^{b-1}[1+b+(1-b)q^b]}{(1+q^b)[a-a(b-1)q^b-(1+q^b)^2]} \quad \text{where} \quad q = |\hat{x}| \tag{18a}$$

$$L'(\hat{r},1) = \frac{a\, b\, \hat{r}^{b-1}[2+b+m+(2-b+m)\hat{r}^b]}{(1+\hat{r}^b)[a-a(b-1)\hat{r}^b-(1+\hat{r}^b)^2]} \quad \text{where} \quad \hat{r} = \sqrt{\hat{x}^2+\hat{y}^2} \tag{18b}$$

The corresponding Pederson conductivity expressions are

$$\Sigma_p^{(0)}(\hat{x},\hat{y}) = \Sigma_{p0}^{(0)}(\hat{y})\ \frac{(1+|\hat{x}|^b)^2}{1-a-B_1|\hat{x}|^b+|\hat{x}|^{2b}} \tag{19a}$$

$$\Sigma_p^{(1)}(\hat{x},\hat{y}) = \exp\left\{\frac{a(1+m)}{A_1}\left[2\tan^{-1}\left(\frac{B_1-2\hat{r}^b}{A_1}\right)-\text{sign}(a)\,\pi\right]\right\}\frac{C_0\,\hat{y}^m\,(1+\hat{r}^b)^2}{1-a-B_1\hat{r}^b+\hat{r}^{2b}} \tag{19b}$$

where $A_1 = \sqrt{-a[4b+a(b-1)^2]}$ and $B_1 = -a(b-1)-2$ and $\hat{r} \hat{=} \sqrt{x^2+\hat{y}^2}$. The constants of integration are chosen to yield the background density at large distances where $x \to \infty$. The physically acceptable solutions have b > 0.

Two types of conductivity structures, cavities and enhancements, are described by (19a and 19b). In the parameter range $\dfrac{-4b}{(b-1)^2} \equiv a_{Min} > a > 0$, the plasma structure is a cavity centered at x = 0. These limits are found by solving for $A_1 = 0$. As parameter "a" approaches the value of "a_{min}" the sides of the density cavity becomes steeper. With a = a_{min}, the wall of the cavity is located at radius is $\hat{r} = \left(\dfrac{b+1}{b-1}\right)^{\frac{1}{b}}$. For b > m + 2, the cavity has a ridge located at

$$\hat{r} = \left(\frac{b+m+2}{b-m-2}\right)^{\frac{1}{b}}.$$

With 0 > a > 1, a conductivity enhancement is found at the origin. This enhancement can represent the increased Pedersen conductivity produced by an artificial ion cloud from Barium or similar material released in the sunlit ionosphere. As a → 1, the sides of the density enhancement become steeper. Solutions exist for all values of b > 0 but if b > 1, the potential vanishes at large distances. If a > 1, then the solutions in (19a and 19b) become complex and are not physically possible. The maximum upward velocity for the potential

$\hat{\Phi}^{(1)}(x, y)$ in (17b) is $V_{y0} = \frac{1}{B_0} \frac{\partial \Phi(x, y, t)}{\partial x} = \frac{a\, E_{Tx}}{B_0}$. If $a > 1$, then the conductivity would move with a velocity larger than the E_{Tx}/B_0 velocity of the driving force, which is not possible. For instance if only a vertical wind U_y is considered in the equation (6) for E_{Tx}, then the upward velocity is $Vy0 = a\, U_y$. An unreasonable value of $a > 1$ would permit the conductivity enhancement to rise faster than the neutral wind driver.

The restrictions on the ranges for the potential amplitude "a" indicate that not all electric potentials correspond to a physical density or Pedersen conductivity structure. For a given force on the plasma from external electric fields, neutral winds or gravity, the induced potential is determined by the gradients on the wall of density cavity or enhancement. These gradients are physically limited by infinite steepness and the amplitude of the potential is a maximum at this limit. Thus, for the solution to (4), a given physical density structure will always correspond to a potential function. The magnitude of a potential function can be increased to the point that there is no corresponding plasma density function.

The one dimensional expression (19a) can represent a horizontal density modulation that uniformly changes the background density of a stratified ionosphere. These may be produced by horizontally traveling acoustic-gravity waves can act as seeds for equatorial bubbles. The elongated shapes of these modulations are illustrated by the example in Figure 2. The elongations can be found in nature as the extensions of an ionospheric plume below its top. The horizontal electric field vectors calculated as gradients of the potential yield vertical plasma transport. This transport is normal to the density gradients and, consequently, no net change in the densities is produced. The electric fields near the top of the bubble are the primary drivers for plasma transport.

The two-dimensional solutions to the potential equation are more useful than the one-dimensional solutions. The expression for $\Sigma_p^{(1)}(\hat{x}, \hat{y})$ in (19b) describes a plasma disturbance with two-dimensional structure. The conductivity (or electron density) vanishes in $\Sigma_p^{(1)}(\hat{x}, \hat{y})$ at y=0 unless m=0. Figure 3 illustrates three examples of the analytic density cavities and the associated electric potential for a uniform background using m = 0. By changing the parameters in the analytic model, a wide variety of density structures is obtained.

The background plasma variation can be approximated using nonzero values of m. The Pedersen conductivity from (19b) vanishes at the $\hat{y} = 0$ boundary if m > 0. With $\Sigma_P = 0$ at the lower $\hat{y}=0$ boundary, the potential equation (7) reduces to $\frac{\partial \Sigma_P}{\partial \hat{y}} \frac{\partial \hat{\Phi}}{\partial \hat{y}} = 0$. To satisfy this condition, $\partial \hat{\Phi}/\partial \hat{y} = 0$ because vertical gradient $\partial \Sigma_p / \partial \hat{y}$ is nonzero-positive at the lower boundary. This condition is automatically built into the analytic expression for the electric potential because of the $\hat{y}^2$ symmetry of $\hat{\Phi}(\hat{x}, \hat{y}) = \hat{x}\, G(\sqrt{\hat{x}^2 + \hat{y}^2})$.

Pedersen Conductivity   Normalized Potential
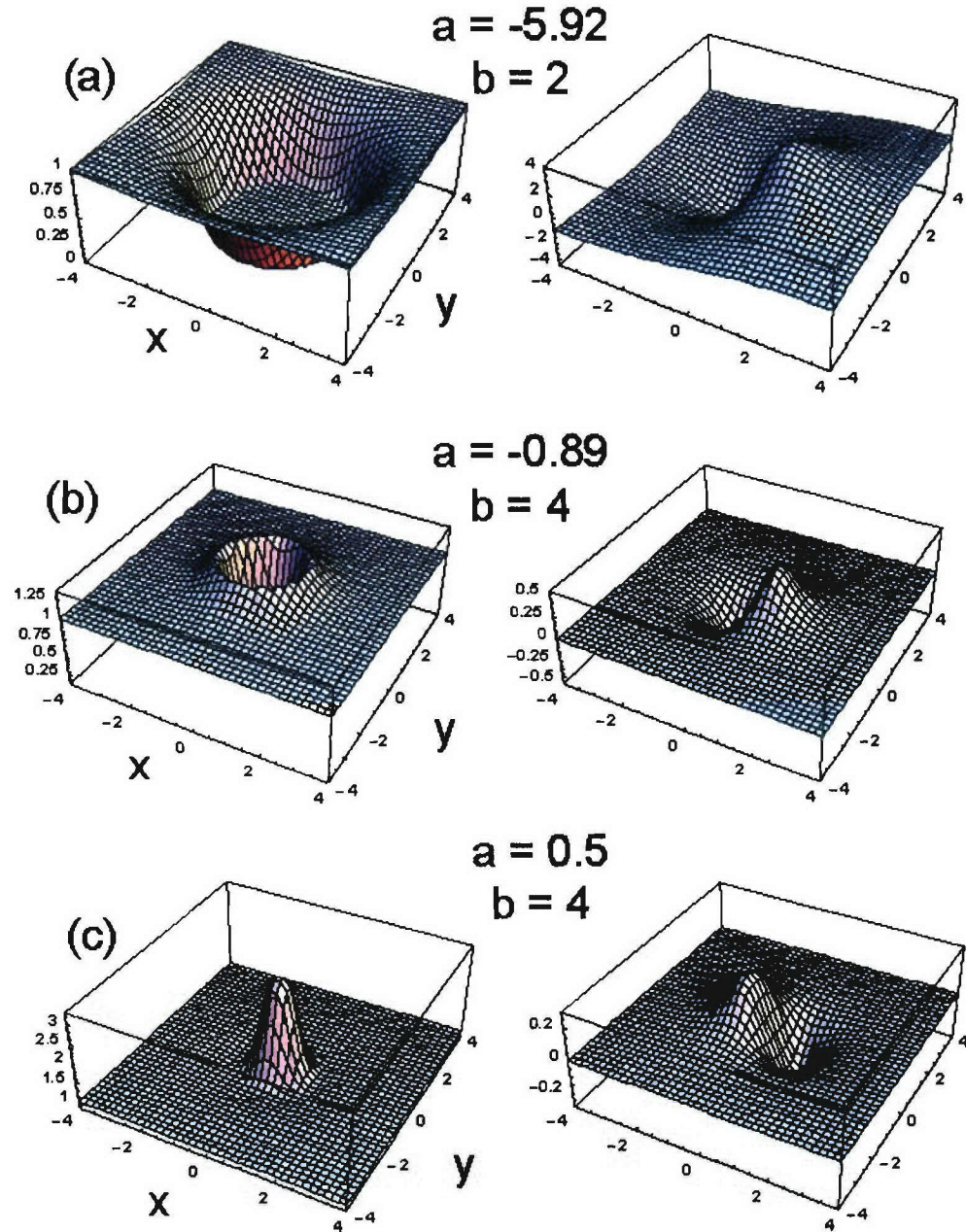
a = -5.92
b = 2

a = -0.89
b = 4

a = 0.5
b = 4

Figure 3. Analytic results for density cavities and enhancements in a uniform background (i.e., m=0). The densities and potentials are computed using (a) b = 2 , a = 0.99 a_{Min} = -5.92, and (b) b =89, a = 0.5 a_{Min} = -0.48, (c) b = 4, a = 0.5. The changes in the parameters yield either (a) a cavity with steep sides, (b) a ridge around the cavity or (c) a peaked enhancement.

12

Two quantitatively different ionospheres can become polarized with the same potential variation. Figure 4 illustrates two solutions of (19b) with identical parameters for a and b but with (a) m = 1 for a linear background profile, and (b) m = 0.25 for a forth-root of y profile. As seen by the solutions in (19a and 19b), a family of Pedersen conductivity structures can be associated with a single electric potential (or field) distribution. This non-uniqueness property can be exploited for modeling the evolution of the density structures

Pedersen Conductivity

Normalized Potential
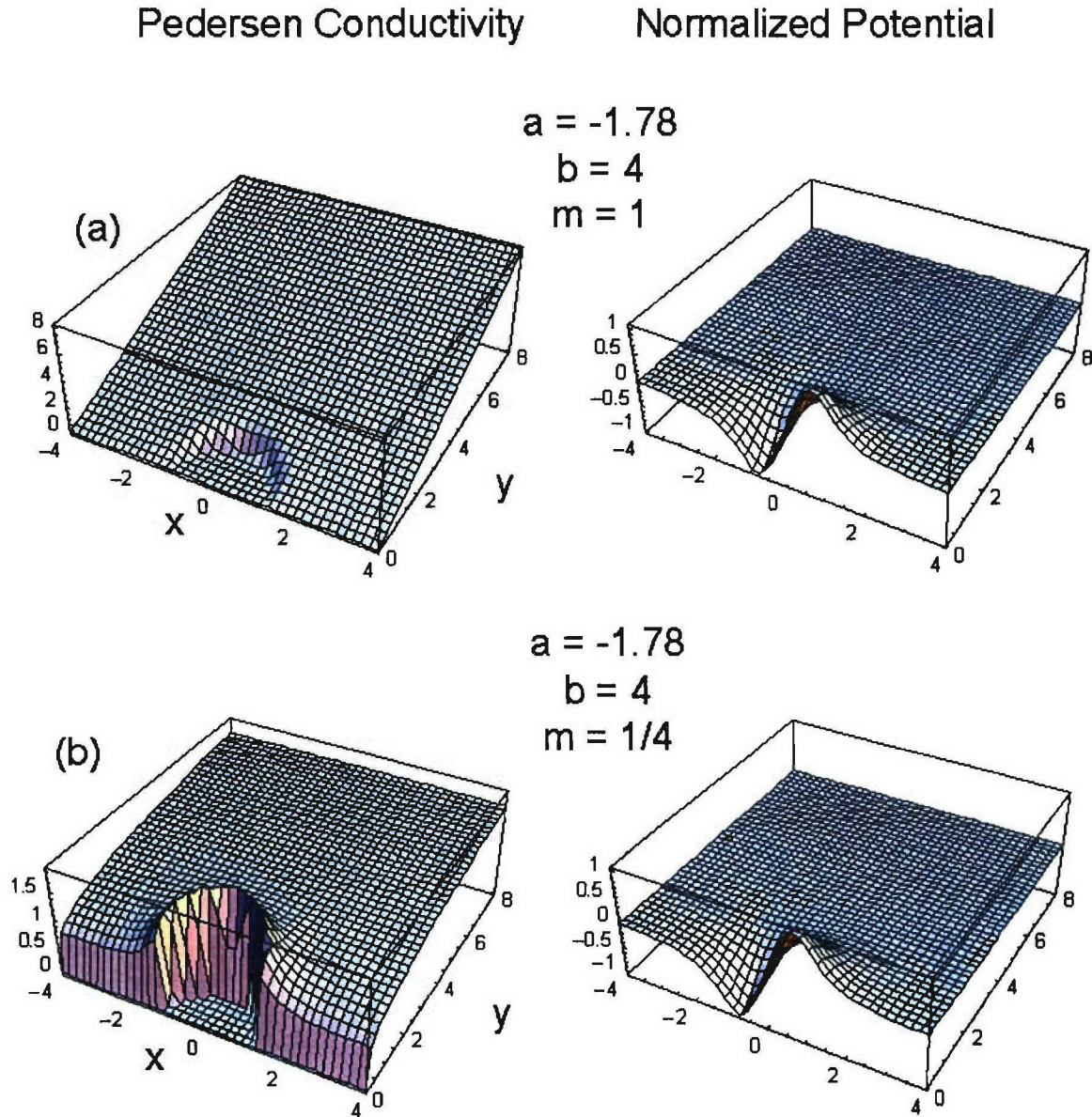
a = -1.78
b = 4
m = 1

a = -1.78
b = 4
m = 1/4

Figure 4. Density cavities imbedded in a linear and inverse-quartic variation for the vertical profile of the plasma conductivity. Both structures yield the same electric potential. The conductivity and the y-directed electric field goes to zero a the lower boundary.

13

One use of the analytic solutions to the potential equation (7) is to provide test cases for the numerical solutions of the same equation. Numerical solutions are influenced by (1) the finite difference approximations to the derivatives, (2) the boundary conditions, and (3) the convergence error for iterative solvers. A direct numerical solver was used to solve for the potential (Appendix A). The Pedersen conductivity was specified using the second, two-dimensional analytic model in (19) with the parameters a = -0.53, b = 4, and m = 1. The

analytic potential $\hat{\Phi}^{(1)}(\hat{x}, \hat{y}) = \dfrac{\hat{x}\, a}{1 + (\hat{x}^2 + \hat{y}^2)^{b/2}}$ from (17b) is compared in Figure 5 with the

numerical solutions for the potential with a variety of boundary conditions.

For uniform boundary densities as illustrated in Figure 3, doubly periodic, doubly fixed (or Dirichlet) [with the boundary potential set to $\hat{\Phi} = 0$], or doubly derivative (or Neumann) [with $\partial\hat{\Phi}/\partial\hat{x} = 0$ and $\partial\hat{\Phi}/\partial\hat{y} = 0$ normal to each boundary] specifications work well. The non-uniformities for the Pedersen conductivities at the boundaries in Figures 4 and 5 require care in the selection of the boundary conditions for numerical solutions. The Pedersen conductivity and corresponding analytic potential are shown in Figures 5a and 5b, respectively. As illustrated by Figures 5c and 5d, inaccurate solutions are obtained for the potential with boundaries specified as doubly periodic and doubly fixed/Dirichlet ($\hat{\Phi} = 0$), respectively. These two boundary conditions force equal potentials at the top and bottom where the real densities are different. Neumann (i.e., zero derivative) boundary conditions yield a useful solution (Figure 5e). Another accurate solution is obtained by using a Neumann (i.e., zero derivative) boundary at the bottom, a Dirichlet (i.e., zero potential) boundary at the top and periodic boundaries at the sides of the solution space (Figure 5f). Table II lists the maximum potential for each solution using a 64 x 32 grid. All of the numerical solutions with the correct shape (Figures 4e and 4f) yield a computed potential that is about 11 % less than the actual values. This reduction is the result of the finite difference approximations for the derivatives in (7).

As the number of mesh points is increased, the numerical solution becomes more accurate. Table III shows the effect of the grid size on the maxima of the computed potentials. The numerical solutions use an n_x by n_y grid in the $\hat{x}$- and $\hat{y}$-directions, respectively. In all cases, the doubly derivative or Neumann boundaries yield slightly better solutions than the mixed boundary solution with doubly periodic in the $\hat{x}$-direction and Neumann/Dirichlet (derivative/fixed) boundary values in the $\hat{y}$-direction. These examples illustrate that the analytic solution pair (17b) and (19b) provides an easy way for testing (1) the utility of the numerical solutions with various boundary conditions and mesh sizes and (2) that the error in the numerical solution vanishes as the grid becomes denser.
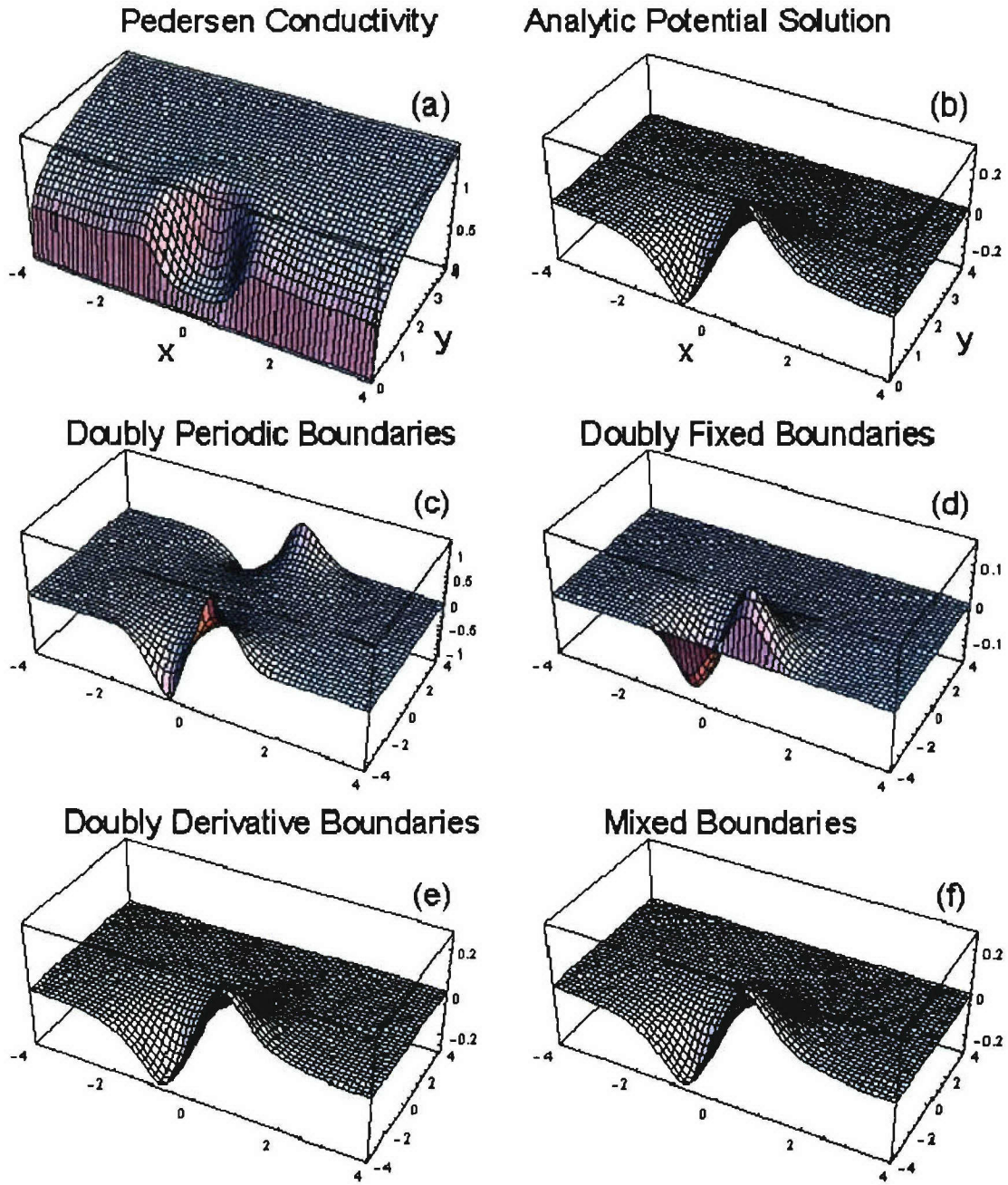
Figure 5. Comparison of analytic and numerical solutions for the electric potential with a density cavity at the bottom side of the stratified plasma. The potential is set up with either downward gravity and winds or horizontal background electric fields. The magnetic field is in the z-direction perpendicular to the horizontal x-axis and vertical y-axis. Analytic solutions for (a) the normalized Pedersen conductivity and (b) the normalized analytic potential are compared to the numerical solutions for the potential with (c) x-periodic and y-periodic boundaries, (d) x-fixed/Dirichlet and y-fixed/Dirichlet boundaries, (3) x-derivative/Neumann and y-derivative/Neumann boundaries, (f) x- derivative/Neumann at bottom, x-fixed/Dirichlet at top and y-periodic boundaries. The latter two boundary conditions yield numerical solutions that approximate the analytic model.

15

The analytic solutions provide a quantitative test of numerical algorithms for the non-separable PDE's that describe electric potentials in the ionosphere. All numerical solvers use the approximations of (1) finitely spaced solution samples (2) boundaries at finite distances. The analytic solution provides infinite spatial resolution with no boundary limits. Test cases can be set up to show the effects on the numerical solutions of boundary placement and boundary types as well as discrete sampling of the coordinate system.

Table II. Error Analysis for Numerically Derived Potentials

Solution	x-Boundary Condition	y-Boundary Condition	Maximum Potential	Maximum Error	Shape	Fig. 3 Panel
Analytic	--	--	0.304	0	Correct	b
Numerical	Periodic	Periodic	1.167	0.863	Incorrect	c
Numerical	Fixed	Fixed	0.154	0.150	Incorrect	d
Numerical	$\partial\hat\Phi/\partial x = 0$	$\partial\hat\Phi/\partial y = 0$	0.273	0.031	Correct	e
Numerical	$\partial\hat\Phi/\partial x = 0$	$\partial\hat\Phi/\partial y = 0$/Fixed	0.271	0.033	Correct	--
Numerical	Fixed	$\partial\hat\Phi/\partial y = 0$/Fixed	0.269	0.035	Correct	--
Numerical	Periodic	$\partial\hat\Phi/\partial y = 0$/Fixed	0.269	0.035	Correct	f

Table III. Mesh Size Affects on Numerically Derived Potentials

Number of Cells in $\hat{x}$-Direction: n_x	Number of Cells in $\hat{y}$-Direction: n_y	Maximum Potential (% Error)	
		Derivative Boundaries	Mixed Boundaries
32	15	0.238 (22 %)	0.236 (22 %)
64	32	0.273 (10 %)	0.269 (12 %)
128	64	0.292 (4 %)	0.286 (6 %)
256	128	0.301 (1 %)	0.296 (3 %)

In summary, exact analytic solutions have been found for the nonlinear potential equation commonly used for determination of electric fields for ionospheric plasma irregularities. These solutions provide easy means to calculate the distributions of plasma conductivity associated with analytic models for the electric potential. These solutions can represent plasma depletions or enhancements depending on the model parameters. The analytic examples demonstrate that a large family of density structures can correspond to identical electric potentials. Also, if the amplitude of a potential is too large, there will not be any corresponding electron density structure. One use of the analytic solutions is to test numerical techniques to solve for the electric potential associated with arbitrary distributions of electron density under the influence of gravity, winds, and ambient electric fields. The next step to complete the quasi-analytic bubble model is to use the exact forms of the electric potential derived in this section to provide transport of the plasma structures. This is described in the next section.

IV.   Quasi-Analytic Solutions for Plasma Transport in a Disturbed Ionosphere

Plasma densities evolve by transport, compression, production and loss. These processes are contained in the continuity equation

$$\frac{\partial n}{\partial t} + \nabla \cdot (nv) = P - L \qquad (20)$$

where n is density, P is production and L is loss. Numerical or analytic solutions to (20) can be based on either the Eulerian or the Lagrangean form of the equations [Richtmyer and Morton, 1967]. These forms are equivalent except the Lagrangean form describes where each bit of fluid cam from originally. Equation (20) is the Eulerian from of the equation of continuity. The Lagrangean from is derived for the special case of incompressible flow.

The compressibility of a plasma is given by the term $\nabla \cdot \mathbf{v}$. When this term is zero, the plasma is termed incompressible. Using (1) the compressibility of the F-region plasma is found to vanish because

$$\nabla \cdot \mathbf{v} = -\nabla \cdot (\nabla \Phi \times \mathbf{B})/B_0^2 = [-\mathbf{B} \cdot (\nabla \times \nabla \Phi) + \nabla \Phi \cdot (\nabla \times \mathbf{B})]/B_0^2 = 0 \qquad (21)$$

where a constant $\mathbf{B}$ is assumed.

Expanding (20) with (21) yields the compressionless form of the continuity equation

$$\frac{\partial n}{\partial t} + \mathbf{v} \cdot \nabla n = \left(\frac{\partial}{\partial t} + \mathbf{v} \cdot \nabla \right) n \equiv \frac{Dn}{Dt} = P - L \qquad (22)$$

where Dn/Dt is called the total derivative. The total derivative of the density moves with a small volume element $(\Delta x, \Delta y, \Delta z)$ in the velocity field. During this process a plasma element at (x, y, z) is mapped to another location (x', y', z') in an increment of time Δt. The incremental mapping equation is given by

$$\mathbf{x}' = \mathbf{x} + \mathbf{v}(\mathbf{x})\Delta t \qquad (23)$$

where the vectors have components $\mathbf{x} = (x, y, z)$ and $\mathbf{v} = (v_x, v_y, v_z)$. The derivative form of (23) simplifies (22) so that

$$\frac{dn(\mathbf{x}, t)}{dt} = P(\mathbf{x}, t) - L(\mathbf{x}, t)$$

$$\frac{d\mathbf{x}(t)}{dt} = \mathbf{v}(\mathbf{x}, t) \qquad (24)$$

If production and loss are neglected, then the electric fields simply move volume elements of plasma in space but the density in each element remains unchanged. Equations (24) are the Lagrangean form of the continuity equation.

An analytic formulation is developed to describe the equatorial bubbles in terms of a mapping function that distorts the ionospheric layer according to the second equation in (24). The mapping function is usually determined with a numerical simulation that calculates the electrostatic $\mathbf{E}$ fields as a function of time and space as an ionospheric bubble or irregularity is formed in the F-layer. Substitution of these fields into (1) yields the transport velocities and the second equation in (24) can be solved to provide the motion of the density coordinates. The transformation of coordinates by this process is given by

$$\mathbf{x}(t) = \mathbf{M}[\mathbf{x}(t_0), t - t_0] \quad \text{and} \quad \mathbf{x}(t_0) = \mathbf{M}^{-1}[\mathbf{x}(t), t - t_0] \tag{25}$$

and, neglecting production and loss, the electron densities are given by

$$n(\mathbf{x}, t) = n(\mathbf{M}^{-1}[\mathbf{x}, t - t_0], t_0) \tag{26}$$

where the map $\mathbf{M}^{-1}$ transforms the distorted coordinates back to the initial coordinate locations.

Taking the magnetic field to be aligned with the z-direction, the electron density fluctuations are assumed to vary in the 2-dimensional coordinate system (x, y). The coordinate transform map is given as

$$\begin{bmatrix} x(t) \\ y(t) \end{bmatrix} = \begin{bmatrix} M_x(x_0, y_0, t - t_0) \\ M_y(x_0, y_0, t - t_0) \end{bmatrix} \tag{27}$$

where y is altitude, x is zonal distance in a flat earth system and (x_0, y_0) are the initial values for these coordinates at time t_0.

The mapping function $\mathbf{M}(x, y, t)$ must be one-to-one and invertible and be the identity map where the induced electric potential is zero and the plasma densities are unchanged. Substitution of (1) into (24) yields

$$\frac{d\mathbf{x}(t)}{dt} = -\frac{\nabla\Phi \times \mathbf{B}}{B_0^2} \tag{28}$$

Assuming uniformity along $\mathbf{B}$ in the z-direction, the differential equations governing the coordinated transformations are

$$\frac{\partial x(x_0, y_0, t)}{\partial t} = -\frac{1}{B_0}\frac{\partial\Phi(x, y, t)}{\partial y} \quad \text{and} \quad \frac{\partial y(x_0, y_0, t)}{\partial t} = \frac{1}{B_0}\frac{\partial\Phi(x, y, t)}{\partial x} \tag{29}$$

18

Differentiating (29) by x0 and y0 and using the Poisson's equation

$$\nabla \cdot E = \nabla \cdot (-\nabla \Phi) = -(\frac{\partial^2 \Phi}{\partial x_0^2} + \frac{\partial^2 \Phi}{\partial y_0^2}) \qquad (30)$$

yields the equations for the velocities

$$\frac{\partial(\partial x/\partial t)}{\partial x_0} = -\frac{\partial(\partial y/\partial t)}{\partial y_0} \text{ and } \frac{\partial(\partial x/\partial t)}{\partial y_0} - \frac{\partial(\partial y/\partial t)}{\partial x_0} = -\nabla^2 \Phi \qquad (31)$$

The areas between curves of constant x0 and y0 are preserved in the transformation and the trajectories of the coordinate transformation follow contours of constant $\Phi(x,y)$. The electric potential is setup by gravity, neutral winds and external electric fields.

Consider the coordinate transformation provided by the analytic potential from (17b) in the previous section

$$\Phi(x,y) = \frac{(x/r_0)\, a_x\, r_0\, E_{Tx}}{1 + [(x/r_0)^2 + (y/r_0)^2]^{b/2}} = \frac{\hat{x}\, a_x\, r_0\, E_{Tx}}{1 + \hat{r}^b} \qquad (32)$$

where coordinates $\hat{x}$ and $\hat{y}$ are the Cartesian coordinates normalized by a constant scale factor r_0 and constants a_x and b define the shape of the potential.

The plasma transport velocities are

$$\frac{\partial \hat{x}}{\partial \hat{t}} = \frac{b\, \hat{x}\, \hat{y}\, \hat{r}^{b-2}}{(1 + \hat{r}^b)^2}$$

$$\frac{\partial \hat{y}}{\partial \hat{t}} = \frac{1 - b\, \hat{x}^2\, \hat{r}^{b-2} + \hat{r}^b}{(1 + \hat{r}^b)^2} \qquad (33)$$

where $\hat{t} = \frac{a_x\, E_{Tx}}{r_0 B_0} t$ and $\hat{r} = \sqrt{\hat{x}^2 + \hat{y}^2}$.

The maximum upward velocity at the ($\hat{x} = 0$, $\hat{y} = 0$) origin is given by $V_{y0} = \frac{a_x\, E_{Tx}}{B_0}$,

independent of the potential shape parameter "b". Note that in our example of the downward gravity vector driving the transport, the parameter E_{Tx} from (6) is less than zero and a value of $a_x < 0$ is required to yield an upward velocity. The parameter $a_x < 0$ denotes a density cavity and consequently the center of the cavity is expected to rise against gravity. If the parameter "a_x" were greater than zero, the center of the density enhancement would fall as

expected under the influence of gravity. For the rest of the discussion, only density cavities will be considered.

The sides of a cavity fall under the influence of gravity. The minimum downward velocity of

$$V_{y1} = -\frac{a_x\, E_{Tx}}{B}\frac{(b-1)^2}{4b} = -V_{y0}\frac{(b-1)^2}{4b}$$ is found at $\hat{x} = \pm\left(\frac{b+1}{b-1}\right)^{1/b}$ and $\hat{y} = 0$. The Cartesian

coordinate system is distorted by the potential inside a conductivity cavity so that the center cells move upward and the side cells move downward.

The analytic model potential with $b = 4$ was previously illustrated in Figure 3b. The corresponding vector field for the plasma velocities (Figure 6a) shows the central uplift of the plasma. As a result of this flow, after normalized time $\hat{t} = 1$ the initially square cells become mapped according to the results shown in Figure 6b. The horizontal (red) and vertical (blue) grid lines become distorted by the vortex flow from the potential. Note that the area in each plasma cell remains constant during this process.

Normalized Velocity Field   Distortion of Square Grid Cells
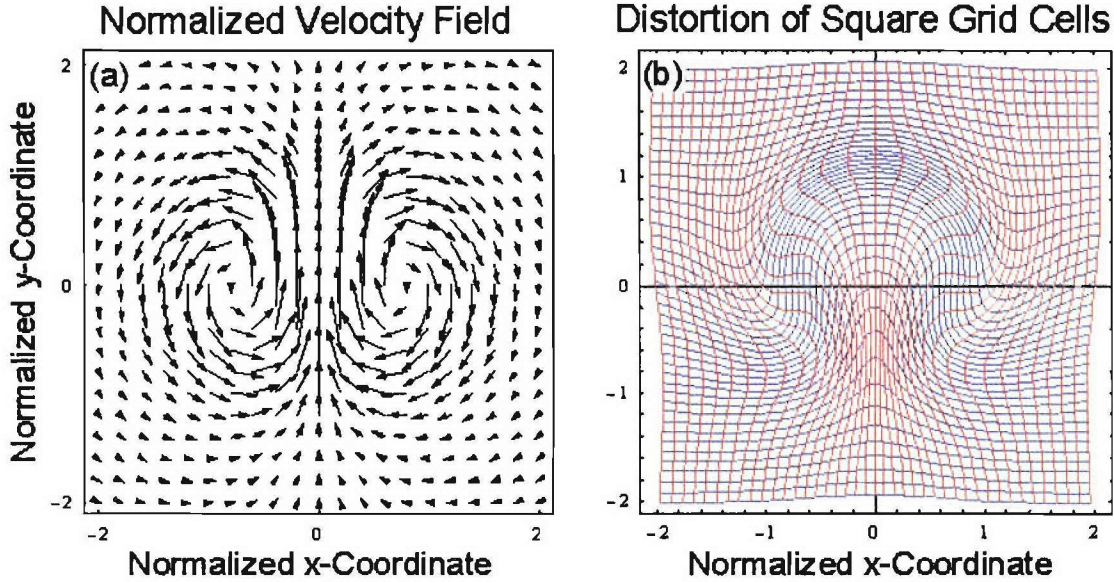
Figure 6. Computed (a) plasma velocities and (b) mapping of Cartesian coordinates by the analytic model for the electric potential shown in Figure 3b. The longest velocity vector has a magnitude $\dfrac{a\,E_{tx}}{B}$ and the spatial coordinates are normalized by the scale length r_0. The coordinate map is illustrated after the flow velocities flow have operated on the plasma for time $t = \left(\dfrac{a\,E_{tx}}{B\,r_0}\right)^{-1}$ or when normalized time $\hat{t} = 1$.

The primary feature of ionospheric bubbles is that they rise leaving an elongated cavity of reduced plasma density often referred to as a "plume". As the plume rises, it carries the

along electric potential. Using the upward velocity for the potential in (32) of $V_{y0} = \dfrac{a_x E_{Tx}}{B_0}$,
the analytic model for the potential becomes

$$\Phi(x,y,t) = \Phi(x,y - V_{y0}t,0) = \frac{x\, a_x\, E_{Tx}}{\left[1 + \left[\left(\dfrac{x}{r_0} \right)^2 + \left(\dfrac{y}{r_0} - \dfrac{V_{y0}t}{r_0} \right)^2 \right] \right]^{b/2}} \cdot \tag{34}$$

With this potential formula, the plasma drift velocities are found from (29) to be

$$\frac{\partial \hat{x}}{\partial \hat{t}} = \hat{x}\,(\hat{y} - \hat{t}) \frac{b\,\left[\hat{x}^2 + (\hat{y} - \hat{t})^2 \right]^{\frac{b-2}{2}}}{\left\{ 1 + \left[\hat{x}^2 + (\hat{y} - \hat{t})^2 \right]^{\frac{b}{2}} \right\}^2}$$

$$\frac{\partial \hat{y}}{\partial \hat{t}} = \frac{1 + [(1-b)\,\hat{x}^2 + (\hat{y} - \hat{t})^2]\left[\hat{x}^2 + (\hat{y} - \hat{t})^2 \right]^{\frac{b-2}{2}}}{\left\{ 1 + \left[\hat{x}^2 + (\hat{y} - \hat{t})^2 \right]^{\frac{b}{2}} \right\}^2} \tag{35}$$

where the time has been normalized by $\hat{t} = t\,V_{y0}/r_0$ and $[\hat{x}(0), \hat{y}(0)] = [\hat{x}_0, \hat{y}_0]$ are the initial conditions at time $\hat{t} \equiv \hat{t}_0 = 0$. This equation is the base for the quasi-analytic transport for production of ionospheric bubbles. By using this equation, it is assumed that the electric potential shape is totally specified with fixed parameters E_{Tx}, a, b, and r_0. The only temporal variation of the potential is that it rises with a constant speed given by

$$V_{y0} = \frac{a_x E_{Tx}}{B_0}.$$

The potential in the trailing portion of the plume is neglected because any vertical flow below the bubble only operates on horizontal gradients and, consequently, there is no net plasma transport within this region.

In the reference frame of the rising potential, $\hat{y}_P \equiv \hat{y} - \hat{t}$ and the differential equations become

$$\frac{\partial \hat{x}}{\partial \hat{t}} = \hat{x}\,\hat{y}_P \frac{b\,\left[\hat{x}^2 + \hat{y}_P^2 \right]^{\frac{b-2}{2}}}{\left\{ 1 + \left[\hat{x}^2 + \hat{y}_P^2 \right]^{\frac{b}{2}} \right\}^2} \quad \text{and} \quad \frac{\partial \hat{y}_P}{\partial \hat{t}} = -1 + \frac{1 + [(1-b)\,\hat{x}^2 + \hat{y}_P^2]\left[\hat{x}^2 + \hat{y}_P^2 \right]^{\frac{b-2}{2}}}{\left\{ 1 + \left[\hat{x}^2 + \hat{y}_P^2 \right]^{\frac{b}{2}} \right\}^2} \tag{36}$$

21

The coordinate transformation if found by integrating (36) for $(\hat{x},\hat{y}_p)$ with an initial value of $(\hat{x}_0,\hat{y}_0)$ and then finding $\hat{y}=\hat{y}_p-\hat{t}$. Further simplification is obtained by transforming to spherical coordinates where $\hat{x}=\hat{r}_p\,Cos\theta_p$ and $\hat{y}_p=\hat{r}_p\,Sin\,\theta_p$. With this substitution, (36) becomes

$$\frac{\partial \hat{r}_P}{\partial \hat{t}} = -\frac{\hat{r}_P^b \sin\theta_P}{1+\hat{r}_P^b}$$

$$\frac{\partial \theta_P}{\partial \hat{t}} = -\frac{\hat{r}_P^{b-1}\cos\theta_P(1+b+\hat{r}_P^b)}{\left(1+\hat{r}_P^b\right)^2}$$

(37)

where the initial conditions at $\hat{t}=0$ are $\hat{r}_P(0)=\sqrt{\hat{x}_0^2+\hat{y}_0^2}$ and $\theta_P(0)=\tan^{-1}(\hat{y}_0/\hat{x}_0)$.

The coordinate transform starts with an electric potential at altitude $\hat{y}\equiv\hat{t}_0=0$ and lets this potential distort the coordinates until time $\hat{t}_1$ when the potential is at altitude $\hat{y}=\hat{t}_1$. The starting and stopping times and altitudes are critical in defining the coordinate distortions. For describing equatorial bubbles, these starting altitude must be transformed to the location where the bubbles starts to form on the bottom side of the ionosphere and the stopping altitude yields with the location of the bubble at time $t_1 = \hat{t}_1\,r_0/V_{y0}$. This renormalization is described later.

The properties of this coordinate transform can be examined at the center where $\hat{x}=0$ and (35) simplifies to

$$\frac{\partial \hat{x}}{\partial \hat{t}} = 0 \text{ with } \hat{x}(0)=\hat{x}(t)=0$$

$$\frac{\partial \hat{y}}{\partial \hat{t}} = \frac{1}{1+\left[(\hat{y}-\hat{t})^2\right]^{\frac{b}{2}}} \text{ with } \hat{y}(0)=\hat{y}_0$$

(38)

The solutions of (38) are found from the nonlinear equation

$$\hat{y}\,\text{Sign}(\hat{y}_0)+\frac{|\hat{y}-\hat{t}|^{1-b}}{1-b} = |\hat{y}_0|+\frac{|\hat{y}_0|^{1-b}}{1-b}$$

(39)

The limiting forms for the asymptotic solutions to (39) are

22

$$\hat{y} \cong \hat{y}_0 \text{ for } \hat{y}_0 < -1$$

$$\left.\begin{array}{l} \hat{y} \cong \hat{y}_0 + \hat{t} \text{ if } \hat{t} < \hat{t}_c \\ \hat{y} \cong \hat{y}_0 + \hat{t}_c \text{ if } \hat{t} > \hat{t}_c \end{array}\right\} \text{ for } -1 < \hat{y}_0 < 0 \text{ and } \hat{t}_c = \frac{(-\hat{y}_0)^{1-b}}{b-1}$$

$$\hat{y} \cong \hat{y}_0 \text{ for } 0 \le \hat{y}_0 \text{ and } \hat{t} < \hat{y}_0$$

$$\hat{y} = \hat{t} \text{ for } \hat{y}_0 = 0 \qquad\qquad (40)$$

$$\hat{y} \cong \hat{t} + \frac{1}{(b-1)^{1/b}} \text{ for } 1 < \hat{y}_0 \text{ and } \hat{t} = \hat{y}_0$$

$$y \cong \hat{t} + \left[(b-1)(\hat{t} - \hat{y}_0) + \hat{y}_0^{1-b}\right]^{\frac{1}{1-b}} \text{ for } 0 < \hat{y}_0 \text{ and } \hat{t} < \hat{y}_0$$

Figure 7. Mapping of the (a) y-axis and (b) a square coordinate grid with a rising potential that starts at the origin. Using equation (34) with b = 4, the coordinates above the initial center of the potential are swept into a narrow band that rises with the upward bubble velocity. The snapshot at $\hat{t} = 6$ shows transport of the ionosphere upward at the center and downward at the sides.

This maps of the coordinate distortions are illustrated in Figure 7 using the potential with index b = 4. The temporal variations in the normalized altitude are given in Figure 7a. The spatial mapping of the grid at time $\hat{t} = 6$ is shown in Figure 7b. The ionosphere is nearly undisturbed below the starting altitude ($\hat{y} = 0$) of the rising electric potential. The ionosphere is also undisturbed for times ($\hat{t} < \hat{y}_0$) when the potential is below the undisturbed ionosphere. As the potential rises, it sweeps up all the coordinates and carries them in a narrow layer at just above the center of the potential function where $\hat{y} = \hat{t}$. This type of coordinate transformation can be used to simulate the rising equatorial bubble. At time $\hat{t}_1$ the potential rises to be centered at an altitude $\hat{y}_1 = \hat{t}_1$.

Figure 8. Coordinate compression at the top of the plasma bubble. For the potential parameters b = 4, the normalized $\hat{y}$-coordinates are mapped to a thin shell about 0.4 to 0.45 above the center of the rising potential function located at $\hat{y} = \hat{t}$.

The horizontal coordinates near the center of the rising potential map to a thin shell centered at the altitude $\hat{y} = \hat{t}$. An approximation to this map is given by the last equation in (22). The evolution of this coordinate "compression" is illustrated in Figure 8 for normalized times between $\hat{t} = 1$ and 20 using the parameter b=4 for the electric potential. The offset ($\hat{y} - \hat{t}$) from the center of the rising bubble increases monotonically but slowly as the initial coordinate covers a much larger range.

24

The normalized density gradient at the edge of the bubble is $\dfrac{\partial n_e}{\partial \hat{y}} = \dfrac{\partial n_e}{\partial \hat{y}_0}\dfrac{\partial \hat{y}_0}{\partial \hat{y}}$ so $\dfrac{\partial \hat{y}_0}{\partial \hat{y}}$ is the coordinate compression factor. Analytically, this factor is given by

$$\frac{\partial \hat{y}_0}{\partial \hat{y}} = \left(\frac{\hat{y}_0}{\hat{y}}\right)^b \frac{1+\hat{y}^b}{1+\hat{y}_0^b} \tag{41}$$

This factor is plotted in Figure 9 with b = 4 for a wide range of times and initial coordinate altitudes. The compression factor increase with time easily attaining values greater than 10 or 100. With this compression, a bottomside ionospheric gradient becomes greatly amplified as the bubble rises.

Figure 9. Density gradient enhancement factor for the coordinate compression at the top of the rising bubble with index b = 4. The compression becomes enhanced with increases in the normalized time $\hat{t}$. Outside the effect of the potential this factor is unity. This processes yields the steepened gradients at the sides of the ionospheric bubble.

To obtain the electron density or Pedersen conductivity at time $(\hat{t})$, cell coordinates must be obtained for the original cell that was transported to the current position. The model ionospheric bubble is therefore formed by operating on a horizontally stratified layer with the *inverse* of the coordinate transformation defined by (35). This inverse may be obtained with by (1) interpolation of the solution to (35) or (2) by reversing time for the solution of (35). Figure 7 shows the location of the coordinates at the current time for each normalized starting position $(\hat{x}_0, \hat{y}_0) \equiv \left(\dfrac{x_0}{r_0}, \dfrac{y_0}{r_0} \right)$. The interpolation process is hampered by the distortion of the coordinate density cells. In the mapping shown by Figure 7b, the square cell with corners at $(\hat{x}_0, \hat{y}_0)$ = (0, 2), (0.1,2), (0.1, 2.1), and (0, 2.1) are mapped to the elongated region with corners (0, 6.421), (0.1075,4.374), (0.1112, 4.443), (0, 6.424) at $\hat{t} = 6$. With linear interpolation, the point $(\hat{x}, \hat{y})$ = (0.055, 5.4) inside the elongated region is determined to map to the initial position $(\hat{x}_0, \hat{y}_0)$ = {0.0505, 2.0364). This is in error; the correct location for this position is $(\hat{x}_0, \hat{y}_0)$ = (0.3329, -0.1784). Beside being prone to error, this technique requires interpolation on a non-uniform mesh or numerical solution for the inverse of interpolation on an a uniformly spaced mesh of the coordinate locations at time $\hat{t} = 0$. For good accuracy and ease of computation, interpolation or numerical inverse solutions should be avoided.

Since the electric potential does not evolve with time, the inverse coordinate mapping is easily achieved with time reversal. Consider a cell with location (x_1, y_1) at time $t = t_1$. Running time backwards to time $t = 0$ yields its starting point (x_0, y_0). If the parameters v_{y0} and b are constant, the time reversal solution is most easily obtained by replacing $\hat{t}$ with $-\hat{t}$ in (35) through (37). This process yields the map represented by (26).

The equations for the inverse coordinate map are

$$\frac{\partial \hat{x}_0}{\partial \hat{t}} = -\hat{x}_0 \, (\hat{y}_0 + \hat{t}) \frac{b \left[\hat{x}_0^{\,2} + (\hat{y}_0 + \hat{t})^2 \right]^{\frac{b-2}{2}}}{\left\{ 1 + \left[\hat{x}_0^{\,2} + (\hat{y}_0 + \hat{t})^2 \right]^{\frac{b}{2}} \right\}^2}$$

$$\frac{\partial \hat{y}_0}{\partial \hat{t}} = - \frac{1 + [(1-b)\,\hat{x}_0^2 + (\hat{y}_0 + \hat{t})^2][\hat{x}_0^2 + (\hat{y}_0 + \hat{t})^2]^{\frac{b-2}{2}}}{\left\{ 1 + \left[\hat{x}_0^2 + (\hat{y}_0 + \hat{t})^2 \right]^{\frac{b}{2}} \right\}^2} \tag{42}$$

The center of the potential function starts at altitude $\hat{y}_0 = \hat{t}_1$ and then (42) solved as the center of the potential falls to an altitude $\hat{y}_0 = 0$. For this reason, the inverse coordinate map equations are integrated from $\hat{t} = -\hat{t}_1$ to $\hat{t} = 0$. The initial conditions for (42) are

$$\hat{x}_0(\text{-}t_1) = \hat{x}_1 \text{ and } \hat{y}_0(\text{-}t_1) = \hat{y}_1 \tag{43}$$

The inverse coordinate map is illustrated in Figure 10 for the initial grid and the distorted inverse grid at several times. This map is used to determine the origin of a coordinate cell and the initial electron density or Pedersen conductivity in that cell. As an example of using this inverse map, the mapping of specific point (0.055, 5.4) is directly obtained with (42) to yield the correct initial location (0.3329, -0.1784).
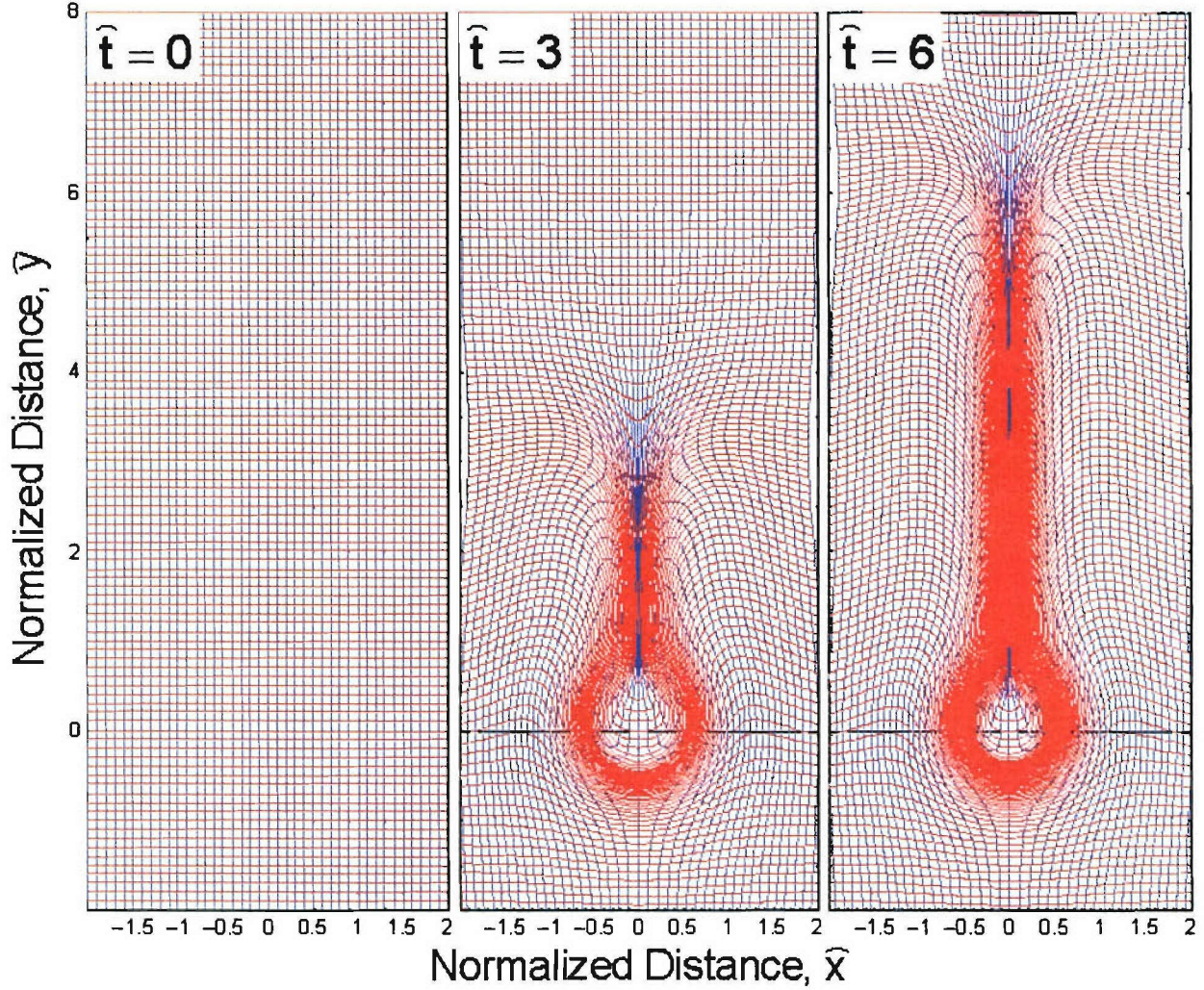

Figure 10. Inverse coordinate map showing source regions for density gradients.

No analytic solution to (42) could be found but the numerical solution to the coupled ordinary differential equations is fast and efficient using standard explicit methods. The Lagrangean inverse-map is consequently called quasi-analytic because no finite-difference approximations are applied to the spatial (x, y) coordinates but discrete steps in the time dependent solutions of (42) is required. Applying the inverse map to any analytical model of a uniform ionosphere can efficiently provide the density at any point in space and time that can be obtained without the use of interpolation or the numerical solution of two-dimensional partial differential equations.

27

As an example, the inverse coordinate map is applied to an F-layer described by the following formula for a modified Chapman layer

$$Ne(y) = Ne_0 \, Exp[1 - z - Exp(z)]$$

$$z = \frac{y - H_P}{H_0} \tag{44}$$

$$H_0 = H_{01} + [0.5 + Tan^{-1}(\frac{y - H_P}{H_1}) / \pi] H_{02}$$

The parameters Ne_0, H_P, H_0, H_{01}, H_{02} and H_1 control the shape of the layer. The analytic simulation uses peak density $Ne_0 = 10^6$ cm^{-3}, peak altitude $H_P = 400$ km, bottom-side scale height $H_{01} = 20$ km, top-side scale height $H_{02} = 50$ km, and transition scale $H_1 = 10$ km. This simple layer model has a steep bottomside representative of the equatorial ionosphere. The conversion from normalized coordinates is $y = \widehat{y} \, r_0 + y_{c0}$ where y_{c0} is the starting altitude of the electric potential at time t = 0.
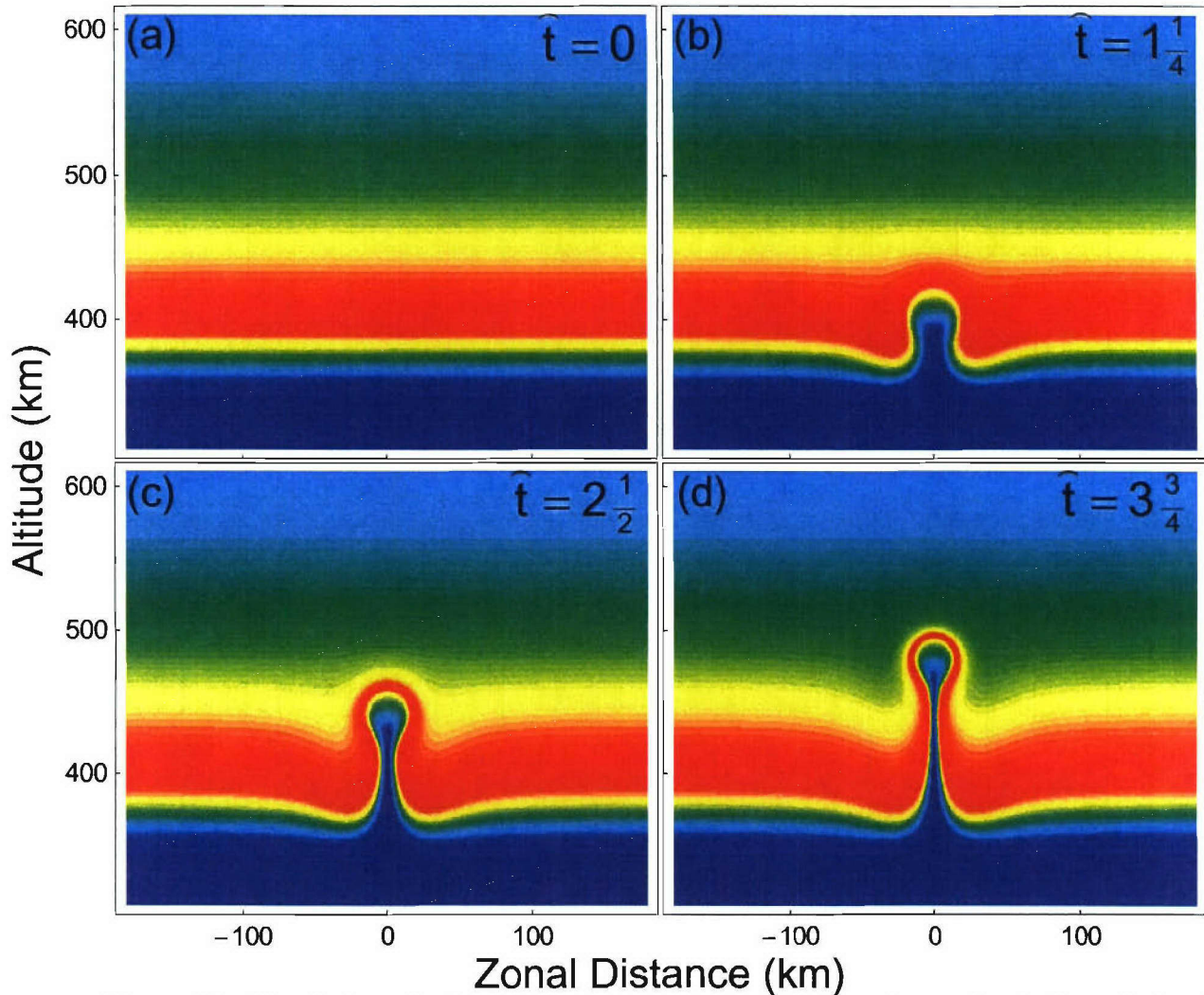

Figure 11. Simulation of a bubble formed in the ionosphere using a simple formulation for the electric potential. The parameters for the model are b=4, and r_0 = 30 km.

Applying the inverse coordinate transformation (42) to the ionospheric profile yields the bubble evolution illustrated in Figure 11. The coordinate distances are determined using a scaling factor $r_0 = 30$ km and the potential function rises through the layer starting at $y_{c0} = 370$ km altitude. The potential function index is arbitrarily set to $b = 4$ for this example. The normalized time coordinate $\hat{t} = t\,V_{y0}/r_0 = t\,a_x\,E_{Tx}/(B\,r_0)$ is used because the parameter "a_x" has yet to be specified. The allowable values for a were previously given after (19) as $\dfrac{-4b}{(b-1)^2} < a < 0$. With a larger value of parameter "$a_x\,E_{Tx}$", the vertical velocity of the bubble increases and the absolute time (t) in the simulation is reduced for a fixed normalized time. Figure 11 illustrates that the analytic model using the rising potential yields a quasi-analytic solution that resembles numerical solutions requiring much more computation time.
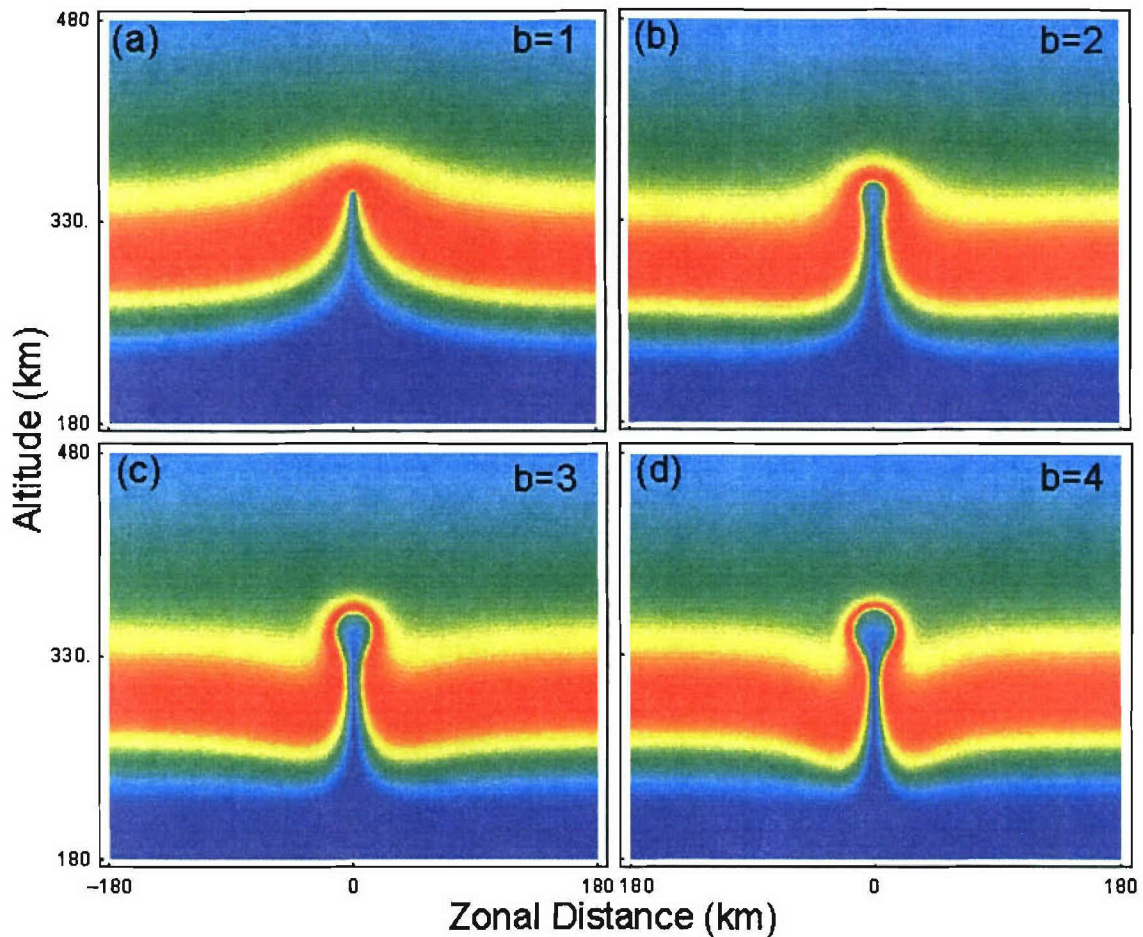

Figure 12. Effect of electric potential index b on the model ionospheric bubble. The normalized time for each solution is $\hat{t} = 3.75$.

Whereas the parameter "a_x" controls the bubble rise rate, the "b" determines the size of the bubble. The parameter "b" may have any value greater than unity. Larger values of b yield

29

electric potentials with larger gradients at the edges. Increasing b increases the region affected by the electric potential. Figure 12 illustrates the ionospheric bubble for several values of this index. Values of the potential index in the range $2 < b < 4$ seem to yield reasonable descriptions of the rising ionospheric bubble.

V.   Bubble Tilts and Ambient Shear Flow

Both observations and numerical computations [Zalesak, Ossakow and Chaturvedi, 1982] have demonstrated that neutral winds can tilt the ionospheric plumes off vertical. When acted on by a zonal neutral wind U_x, a vertical electric field E_y is produce by interactions with the background electron density (or Pedersen conductivity). Also, a perturbation electric field E_{Ty} is produced by polarization of the plasma density bubble by the neutral wind. These two processes work simultaneously to affect the tilt the bubbles. First, the background neutral wind induces large scale plasma motions in the zonal, eastward direction. The shear in this large-scale plasma drift will cause the regions of lower background Pedersen conductivity to lag behind the regions of maximum Pedersen conductivity. Second, polarization of the ionospheric bubbles by the neutral wind, which moves faster than the bulk motion of the plasma, will produce horizontal motion that will cause the density depletions to move in the opposite direction of the neutral wind relative to the bulk plasma drift. This is a well known property of plasma holes as they respond to neutral winds [Bernhardt, 1988]. Both of these processes are easily incorporated in the quasi-analytic bubble model.

Vertical gradients in the background density yield vertical gradients in the induced electric field and vertical shears in the horizontal plasma drifts produced by these fields. This process is captured in (2) assuming that the vertical currents vanish with the result

$$J_y = [E_y - U_x B_0] \sigma_P = 0 \tag{45}$$

The field line is divided into the F-region where the wind is uniform and the E-region where the neutral wind will assume to vanish [Zalesak, Ossakow and Chaturvedi, 1982]. Calling the integrated Pedersen conductivity in these two regions Σ_F and Σ_E respectively, the vertical electric field profile is given by

$$E_y(y) = \frac{U_x B_0 \Sigma_F(y)}{\Sigma_E + \Sigma_F(y)} \equiv -\frac{\partial \Phi_0}{\partial y} \tag{46}$$

where Φ_0 is the polarization potential of the background plasma.

The resulting plasma velocity is given by (24) with the result

$$\frac{\partial x}{\partial t} = \frac{E_y}{B_0} = U_x \frac{\Sigma_F(y)}{\Sigma_E + \Sigma_F(y)} = U_x \frac{1}{\widehat{f}(y/r0) + 1} \equiv V_{xs} \tag{47}$$

30

where $\hat{f}(y/r_0) = \hat{f}(\hat{y}) = \dfrac{\Sigma_E}{\Sigma_F(y/r_0)}$. $\qquad$ (48)

This is the horizontal velocity of the plasma in which the bubble is imbedded. Usually the wind shear variation is small compared to the average bulk motion.

In normalized coordinates, this wind shear equation for the background horizontal motion becomes

$$\frac{\partial \hat{x}}{\partial \hat{t}} = \frac{V_{xS}}{V_{y0}} = \frac{U_x}{V_{y0}} \frac{\Sigma_F(y/r_0)}{\Sigma_E + \Sigma_F(y/r_0)} = \frac{U_x}{V_{y0}} \frac{1}{1+\hat{f}(\hat{y})} \equiv \hat{V}_{xS}(\hat{y}) \qquad (49)$$

Integration of (49) yields the simple coordinate map from this large scale plasma motion

$$\hat{x}(\hat{t}) = \int \hat{V}_{xS}(\hat{y})\, d\hat{t} = \hat{x}_0 + \hat{t}\,\hat{V}_{xS}(\hat{y}) \qquad (50)$$

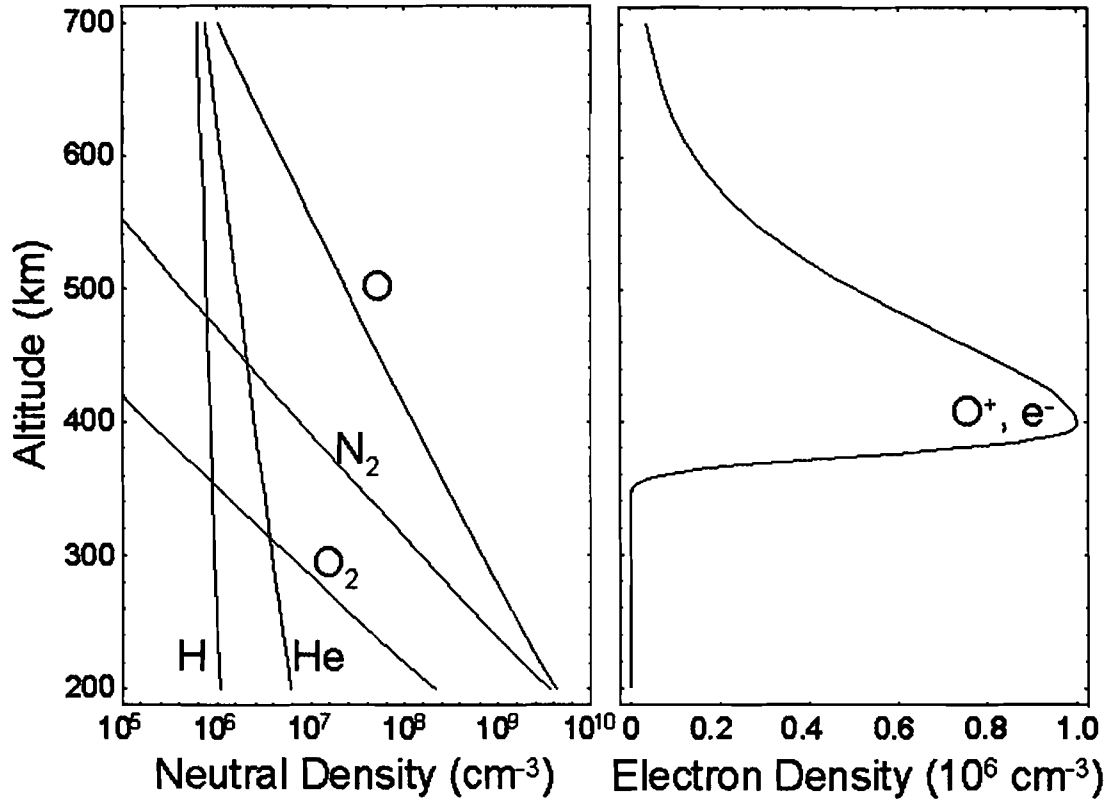where x_0 is the initial coordinate at time $\hat{t} = 0$.

Figure 13. Profiles from neutral atmosphere and electron density models used for the sample computations of electric polarization that tilts the equatorial bubbles.
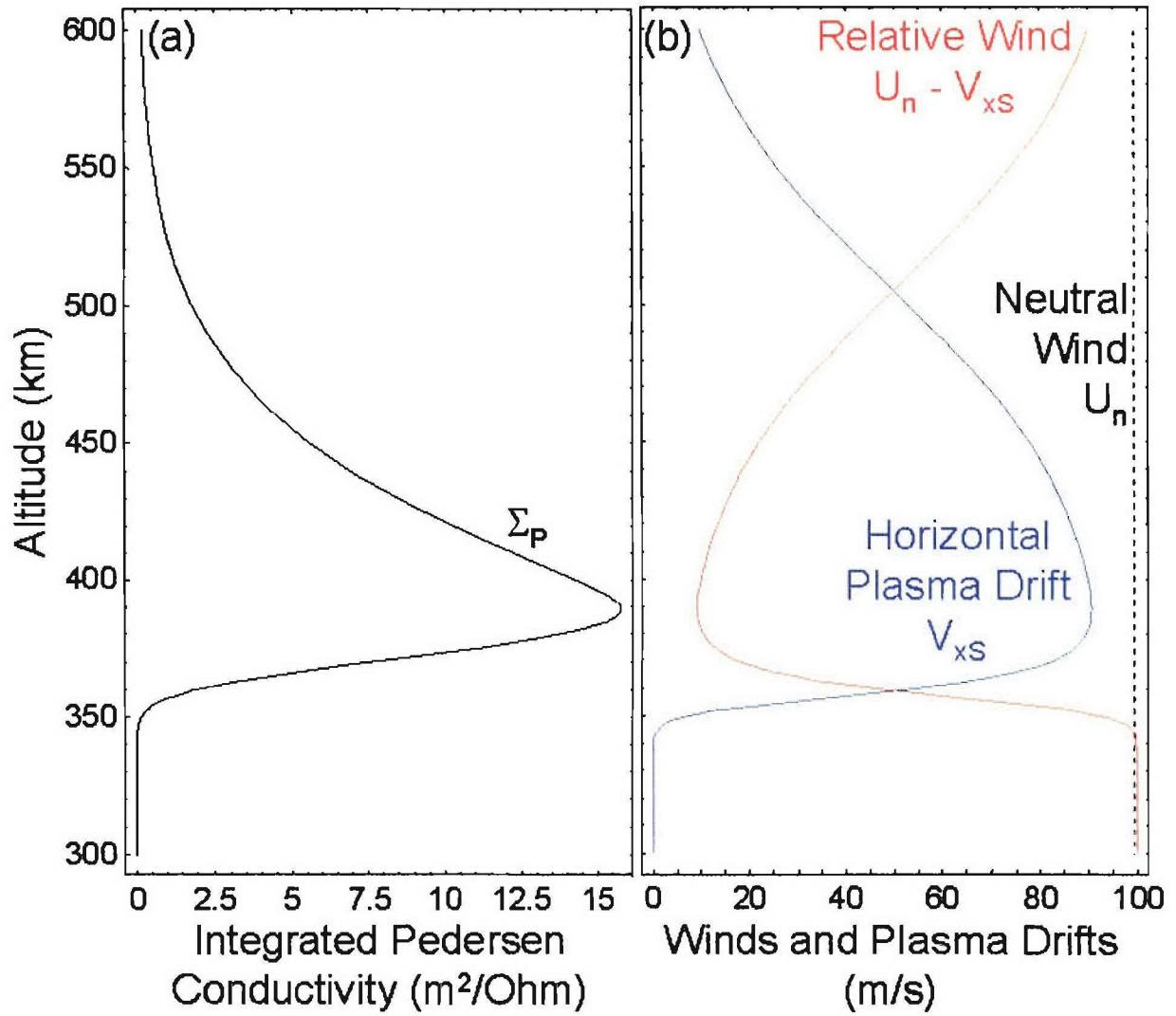
Figure 14. Model profiles of field-line integrated Pedersen conductivity, uniform neutral wind, large-scale horizontal plasma drifts, and horizontal wind relative to the drifting plasma.

If the E-region Pedersen conductivity is zero, then the plasma will move horizontally with the neutral wind speed U_x. A finite Σ_E coupled with vertical shears in the F-region Pedersen conductivity gives a shear structure to the horizontal plasma motion. The tilts of the equatorial plume structures will be computed using the Lagrangean approach to the plasma transport with both imbedded potential given by (34) and the large scale distortions described by (50).

As an example of this wind induced shear in the horizontal plasma drift, a uniform neutral with $U_x = 100$ m/s was used to polarized the plasma layer given by (44) with a peak density of 10^6 cm^{-3}. The model neutral atmosphere and electron density profiles illustrated in Figure 13 are used to derive the equatorial profile of the field-line integrated Pedersen conductivity shown in Figure 14. A dipole magnetic field model of the form

$$B_r = \frac{2\,H_0\,\text{Cos}\theta}{r^3} \text{ and } B_\theta = \frac{H_0\,\text{Sin}\theta}{r^3} \tag{51}$$

is used for the magnetic field lines where H_0 = -0.311 10^{-5} Tesla. Figure 15 illustrates the distortion of a square mesh using the coordinate transform defined by (47). Application of this transform after the transform illustrated in Figure 7 will tilt the bubble to the left (west) side of the simulation. The simulation for Figure 15 used a fixed E-region conductivity Σ_E that was one-tenth the maximum value of the F-layer Pedersen conductivity Σ_F.

100 m/s Neutral Wind ▮▮▮▶ **Plasma Drift (m/s)** ▮▮▮▶ **Horizontal Coordinated Displacement (km)**
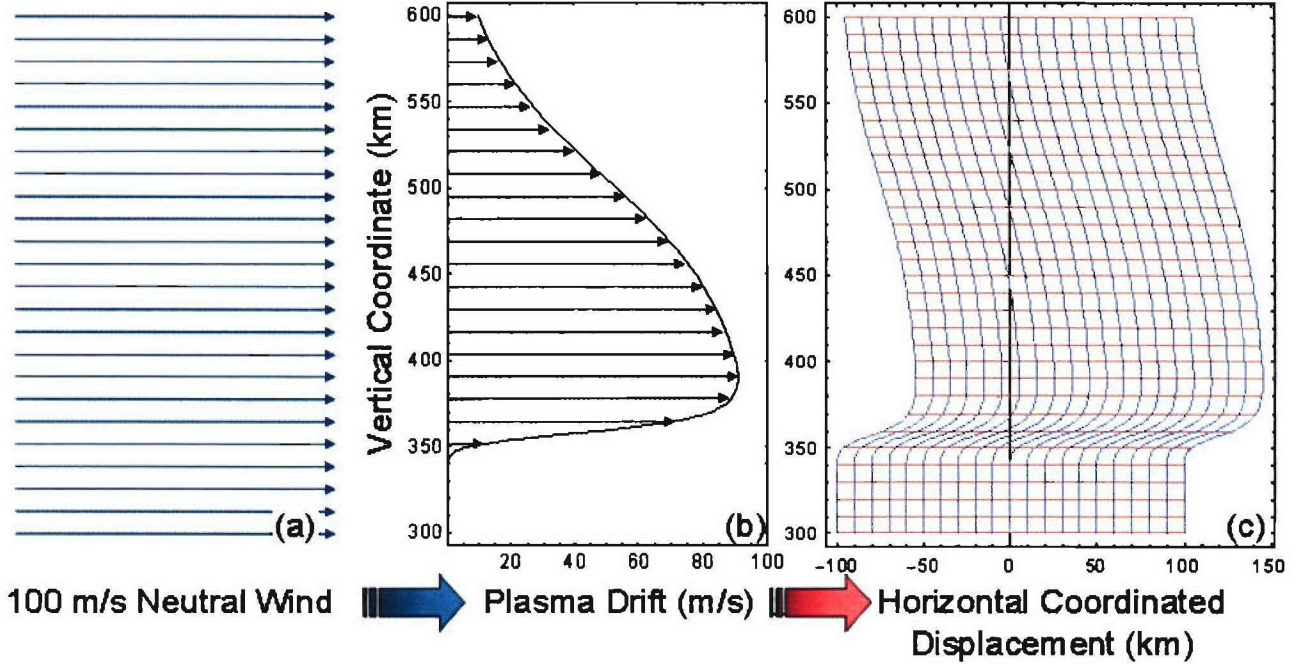
Figure 15. Horizontal coordinate distortion by wind induced plasma shear flow after 500 seconds of plasma motion.

The rising bubble will be caught in the sheared plasma flow to provide a tilt to the bubble. To model this tilt, the quasi-analytic transport model will be modified assuming that the bubble follows a trajectory that is a combination of the vertical rise velocity Vy0 and the horizontal shear velocity given by (47). The equations for the trajectory of the center (x_c, y_c) of the bubble is

$$\frac{\partial y_c}{\partial t} = V_{y0} \text{ and } \frac{\partial x_c}{\partial t} = V_{xS}(y_c) \tag{52}$$

Assuming that the bubble starts to form at the initial location $(x, y) = (0, y_{c0})$, then the solution of (52) becomes

$$y_c = y_{c0} + V_{y0}t \text{ and } x_c = \int_0^t V_{Sx}(y_{c0} + V_{y0}t')\,dt' \tag{53}$$

33

In normalized coordinates this solution for the center trajectory of the bubble becomes

$$\hat{y}_c = \hat{t} \quad \text{and} \quad \hat{x}_c = \int_0^{\hat{t}} \hat{V}_{xS}(\hat{\tau}) \, d\hat{\tau} \tag{54}$$

where distance is normalized by r_0, velocities are normalized by V_{y0} and time is normalized by r_0/V_{y0} as before.

The simple coordinate map (47) neglects horizontal flow from internal polarization of the bubble. This flow is the result of vertical polarization fields generated by polarization of the bubble structure by the neutral wind. This process has been described in Section II except that, along with vertical gravitational acceleration, the horizontal neutral wind induces an electric potential that causes horizontal motion of the bubble center. From (6), the vector electric field from these forces is

$$\mathbf{E}_0 + (\mathbf{U} + \frac{\mathbf{g}}{\nu_{in}}) \times \mathbf{B} \equiv -\mathbf{E}_T \tag{56}$$

The horizontal neutral wind in the rest frame of the plasma bubble is $U_x - V_{x0}$ where V_{x0} is the horizontal velocity of the center of the bubble. The electric field associated with this neutral wind in this frame is

$$E_{Ty} \, \hat{y} \equiv (U_x - V_{x0}) B_0 \, \hat{y} \tag{57}$$

by the definition in (56). In the rest frame of the plasma, the relative velocity of the electric potential at altitude $y = y_c$,

$$V_{xR}(y_c) = \frac{E_{Ty}}{B_0} = -\frac{1}{B_0} \frac{\partial \Phi_1}{\partial y} \tag{58}$$

where Φ_1 is the potential from internal polarization.

The response of the plasma to this drive field is dependent on the physical structure of the bubble. For the tilted bubble model with internal polarization, a single parameter scaling of the ambient drifts is used. The horizontal drift velocity of the bubble center is assumed to have the form

$$V_{x0}(y) = (1 - a_y) V_{xS} = V_{xS} + V_{xR} \quad \text{with} \quad V_{xR} = -a_y V_{xS} \tag{59}$$

where a_y is a constant analogous to a_x used in the previous section to determine the bubble rise rate from gravity. The parameter a_y determines the bubble velocity in a rest frame of the background plasma. For density depressions, a_y is less than zero.

The wind and plasma drift profiles in Figure 14 illustrate this polarization effect. Figure 14b shows that, near the peak, the relative wind in the plasma rest frame is about 10% of the total

34

plasma drift. The parameter a_y controls the relative velocity of the bubble in the background plasma. If $a_y = 0$, the bubble drifts with the background plasma as if there were on internal polarization of the bubble. If $a_y = -1$, the background horizontal plasma drift adds to the wind-induced relative motion produced by the polarization fields inside the bubble giving $V_{x0} = 2 V_{xS}$ and $V_{xR} = -V_{xS}$. In normalized coordinates (59) becomes

$$\hat{V}_{x0} = \frac{V_{x0}}{V_{y0}} = (1 - a_y)\hat{V}_{xS} = \hat{V}_{xS} + \hat{V}_{xR} \, . \tag{60}$$

Lin et al., [2005] measure relative zonal propagation of equatorial plasma bubbles that is consistent with this internal polarization effect. Using the definition of

$$a_y = -V_{xR}/V_{xS} \tag{61}$$

where V_{xR} is the measured bubble velocity relative to the background plasma drive V_{xS}, the observations of Lin et al. [2005] yield time dependent values of a_y from 1.7 at 20 magnetic local time (MLT) to 0.3 at 22 MLT. Lin et al [2005], however, attribute this effect to strong coupling between atmospheric gravity waves and the Rayleigh-Taylor instability. This paper asserts that polarization potentials of the density depletions set up by the relative neutral wind can explain the enhanced motion of the bubbles.

The technique for bubble modeling is based on the motion of the analytic electric potential along a trajectory. The tilted bubble rises along the path defined by the velocity $V_0 = V_{x0}\hat{x} + V_{y0}\hat{y}$. With both background drift and internal plasma motion, the dynamics of the center of the plasma bubble potential are given by

$$\frac{\partial y_c}{\partial t} = V_{y0} \quad \text{and} \quad \frac{\partial x_c}{\partial t} = V_{x0} = (1 - a_y)V_{xS} \tag{62}$$

with the initial conditions $[x_c(0), y_c(0)] = [\, 0, \; y_{c0} \,]$.

For the tilted bubble model, the internal horizontal and vertical electric fields are considered along with of the overall motion of the background plasma. With the internal field assumption, the analytical potential function becomes

$$\Phi(x, y, t) = \Phi_0(y) + \Phi_1(x - x_c, y - y_{c0} - V_{y0}t, 0)$$

$$= \Phi_0(y) + B_0 \frac{[x - x_c(t)] V_{y0} - [y - y_{c0} - V_{y0}t] \; V_{xR}(y_{c0} + V_{y0}t)}{\left[1 + \left[\left(\dfrac{x - x_c(t)}{r_0}\right)^2 + \left(\dfrac{y - y_{c0} - V_{y0}t}{r_0}\right)^2\right]\right]^{b/2}} \tag{63}$$

which is identical to (34) with Φ_0, V_{xR} and x_c equal to zero. The induced plasma bubble velocity in the horizontal direction is

$$V_{x0} = -\frac{1}{B_0}\frac{\partial \Phi}{\partial y} = V_{xS} + V_{xR} \tag{64}$$

at the position $x = x_c(t)$ and $y = y_{c0} + V_{y0}t$. The added variables tilt the electric potential off vertical so that the head of the bubble can flow against the ambient drift of the background plasma.

The coordinate shift $x_p = x - x_c(t)$ and $y_p = y - y_{c0} - V_{y0}t$ translates the potential into the reference frame of the bubble center with the result

$$\Phi(x,y,t) = \Phi_0(y) + B_0 \frac{x_p V_{y0} - y_p \, V_{xR}(y_{c0} + V_{y0}t)}{1 + (r_p/r_0)^b} \tag{65}$$

where $r_p^2 = x_p^2 + y_p^2$.

The potential function given by (65) is substituted into the Lagrangean transport equations

$$\frac{\partial x(x_0, y_0, t)}{\partial t} = -\frac{1}{B_0}\frac{\partial \Phi(x,y,t)}{\partial y} \quad \text{and} \quad \frac{\partial y(x_0, y_0, t)}{\partial t} = \frac{1}{B_0}\frac{\partial \Phi(x,y,t)}{\partial x} \tag{66}$$

The resulting coordinate mapping equations for the rising potential in sheared plasma flow is

$$\frac{\partial x_c}{\partial t} = V_{x0}(y_c) = V_{x0}(y_{c0} + V_{y0}t)$$

$$\frac{\partial x}{\partial t} = \frac{b\, r_p^{b-2} r_0^{-b} y_p [x_p V_{y0} - y_p \, V_{xR}(y_{c0} + V_{y0}t)] + [1 + r_p^b r_0^{-b}]V_{xR}(y_{c0} + V_{y0}t)}{(1 + r_p^b \, r_0^{-b})^2} + V_{xS}(y) \tag{66}$$

$$\frac{\partial y}{\partial t} = \frac{V_{y0}[1 + r_p^b r_0^{-b}] - b\, r_p^{b-2} r_0^{-b} x_p [x_p V_{y0} - y_p \, V_{xR}(y_{c0} + V_{y0}t)]}{(1 + r_p^b \, r_0^{-b})^2}$$

incorporating both internal and external forces on the bubble.

In normalized coordinates, the transport equations become

36

$$\frac{\partial \hat{x}_c}{\partial \hat{t}} = V_{x0}(\hat{y}_c), \quad \hat{y}_c = \hat{t},$$

$$\frac{\partial \hat{x}}{\partial \hat{t}} = \frac{b \ \hat{r}_p^{b-2}\hat{y}[\hat{x} - \hat{V}_{sR}(\hat{y}_c)\,\hat{y}] + [1 + \hat{r}_p^b]\,\hat{V}_{sR}(\hat{y}_c)}{[1 + \hat{r}_p^b]^2} + \hat{V}_{xS}(\hat{y})$$

(67)

$$\frac{\partial \hat{y}}{\partial \hat{t}} = \frac{1 + \hat{r}^b - b \ \hat{r}_p^{b-2}\hat{x}\,[\hat{x} - \hat{V}_{sR}(\hat{y}_c)\,\hat{y}]}{[1 + \hat{r}_p^b]^2}$$

where once again distance is normalized by r_0, velocity is normalized by V_{y0}, and time is normalized by r_0/V_{y0}. The velocity functions are all related to the normalized plasma shear by the parameter a_y with $V_{x0}(\hat{y}) /(1 - a_y) = - \hat{V}_{xR}(\hat{y})/a_y = \hat{V}_{xS}(\hat{y})$.

Before computing the coordinate mapping, the trajectory of the center of the potential function (x_c, y_c) is found by solving the first ordinary differential equation in (66) or (67). For this calculation and all the follow, the shear velocity shown in Figure 15 was used in (60) with a several values of a_y. Figure 16 illustrates the model results for the motion of bubble center as a function of the parameter a_y. With $a_y = 0$ the potential will rise and drift east reaching a maximum distance on the topside where the wind induced drift vanishes. As the parameter a_y is increased toward unity, the internal polarization of the bubble inhibits its horizontal motion in the background plasma flow.

To illustrate the results from these coordinate-mapping equations, the parameter a_y is set to one-tenth so the potential function moves horizontally with the ambient plasma flow at each altitude and is slightly retarded by internal polarization. When $a_y = 0.1$, then $V_{xR}(y) = V_{xS}/10$, $V_{x0} = 9 \ V_{xS}/10$. The initial conditions for the coordinate map are $[\hat{x}_c(0), \hat{x}(0), \hat{y}(0)] = [0, \hat{x}_0, \hat{y}_0]$ at $\hat{t} = 0$. All of the results are displayed in normalized coordinates. The normalization parameters $r_0 = 30$ km, and $v_{y0} = 100$ m/s can be used to translate the solutions back to physical space. The bubble moves with the vertical rise velocity from internal electric fields set up by gravity. By setting the internal polarization parameter a_y nearly to zero, the horizontal motion is primarily with the background plasma but there is a small retardation from the internal fields. The shear function was put into normalized form from the physics coordinates using the definition $\hat{y} = (y - y_{c0})/r_0$ where $y_{c0} = 370$ km. With the parameter $b = 4$, the ordinary differential equations given in (67) are integrated in time to yield the quasi-analytic solutions for the Lagrangean coordinate distortions shown in Figure 17. The center of the potential function as derived from the first equation in (67) is shown by the green curve in each figure. The plume structure below the top of the bubble becomes caught up in the ambient flow to from a backwards "C". The successive images in Figure 17 are normalized shown for normalized times of 2, 4, and 6. Using the normalization factor $r_0/V_{y0} = 300$ seconds, the absolute times for the tilted bubble coordinate maps are (a) 600, (b) 1200, and (c) 1800 seconds.
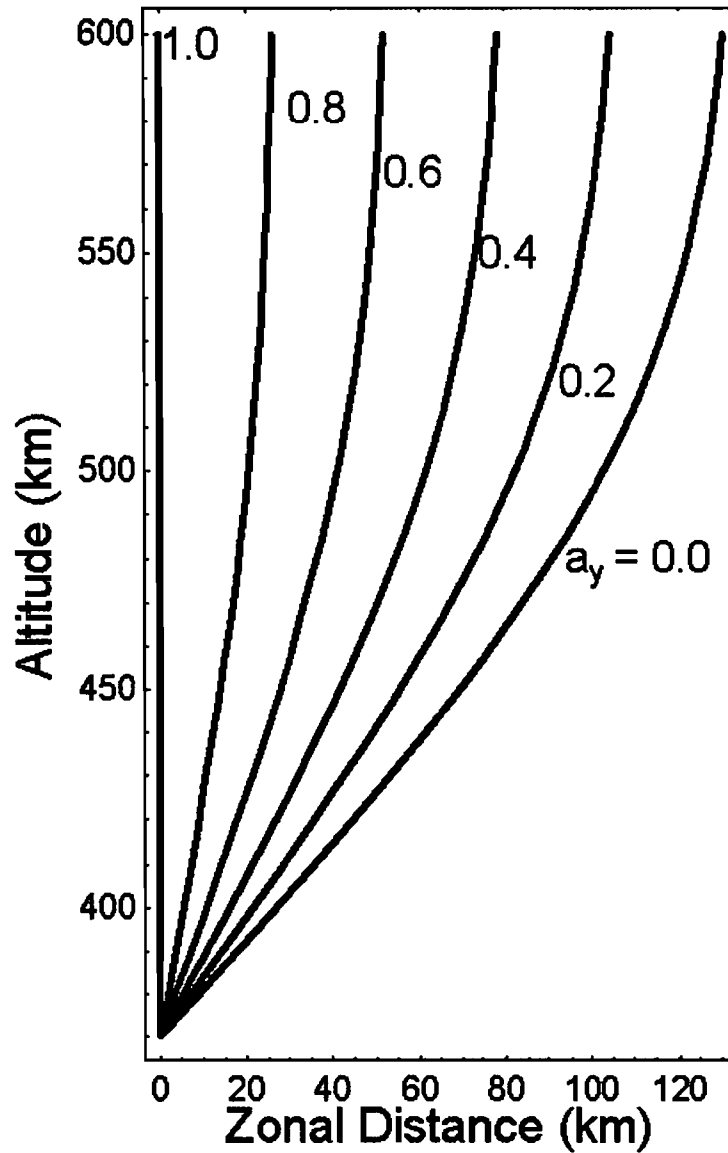
Figure 16. Curves of the trajectory for the analytic potential function used to create the equatorial bubble. With parameter $a_y = 0$, the internal polarization of the bubble is neglected and the potential function is transported by the full action of the plasma shear. As a_y is increased, the zonal motion of the center of the bubble potential is reduced. With $a_y = 1$, the internal polarization at the head of the bubble completely cancels the plasma drift of the ambient layer.
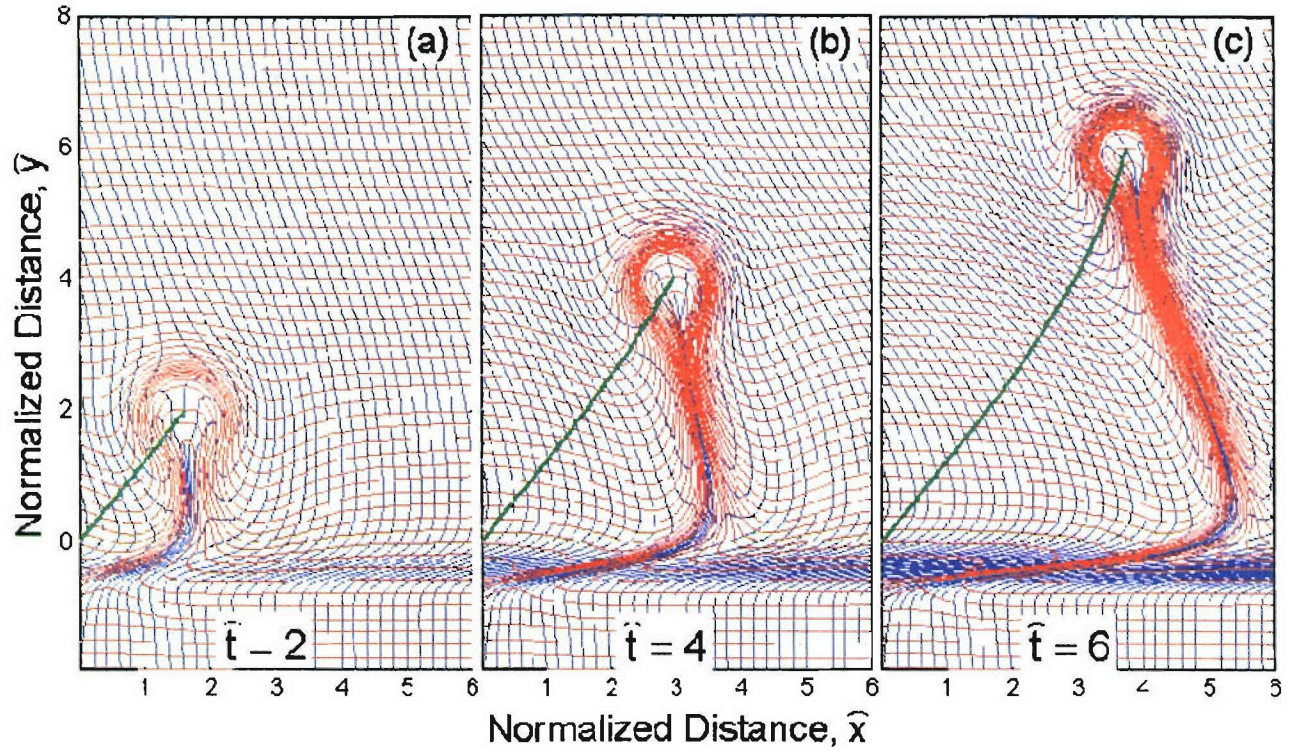
Figure 17 Coordinate map for distortions from a rising (b = 4) bubble in a sheared background plasma flow. The green line shows the trajectory of the center of the bubble with $a_y = 0.1$. The plume becomes curved as it is caught in the ambient plasma flow.

The coordinate transform equations in (67) yield the normalized, destination coordinates $[\hat{x}(\hat{t}), \hat{y}(\hat{t})]$ from the given initial coordinates $[\hat{x}_0, \hat{y}_0]$. To determine a mapped density at a given location, the time-inverse transformation to determine the initial coordinates for a coordinate cell that is transported to a given location. This inverse transform has already been discussed in the previous section for bubbles with out tilts. This inverse map are obtained by replacing t with –t in (67). The center of the potential function starts at location $\hat{x}_0 = x_c(\hat{t}_1)$ and $\hat{y}_0 = \hat{t}_1$.

The solution for the inverse coordinate transform proceeds in two steps. First, the initial equation in (67) is solved to yield the function $x_c(t)$ for the horizontal displacement of the bubble potential function. Next, the system given by (68) is integrated as the potential follows a trajectory $[\hat{x}_c(\hat{t}), \hat{y}_c(\hat{t})]$ to end at the origin of the normalized coordinate system where $\hat{x}_0 = 0$ and $\hat{y}_0 = 0$. The curves in Figure 16 show the $[\hat{x}_c(\hat{t}), \hat{y}_c(\hat{t})]$ trajectories as a function of the internal polarization factor a_y. As previously discussed with (42), the inverse coordinate map equations are integrated from $\hat{t} = -\hat{t}_1$ to $\hat{t} = 0$. The initial conditions for (63) are

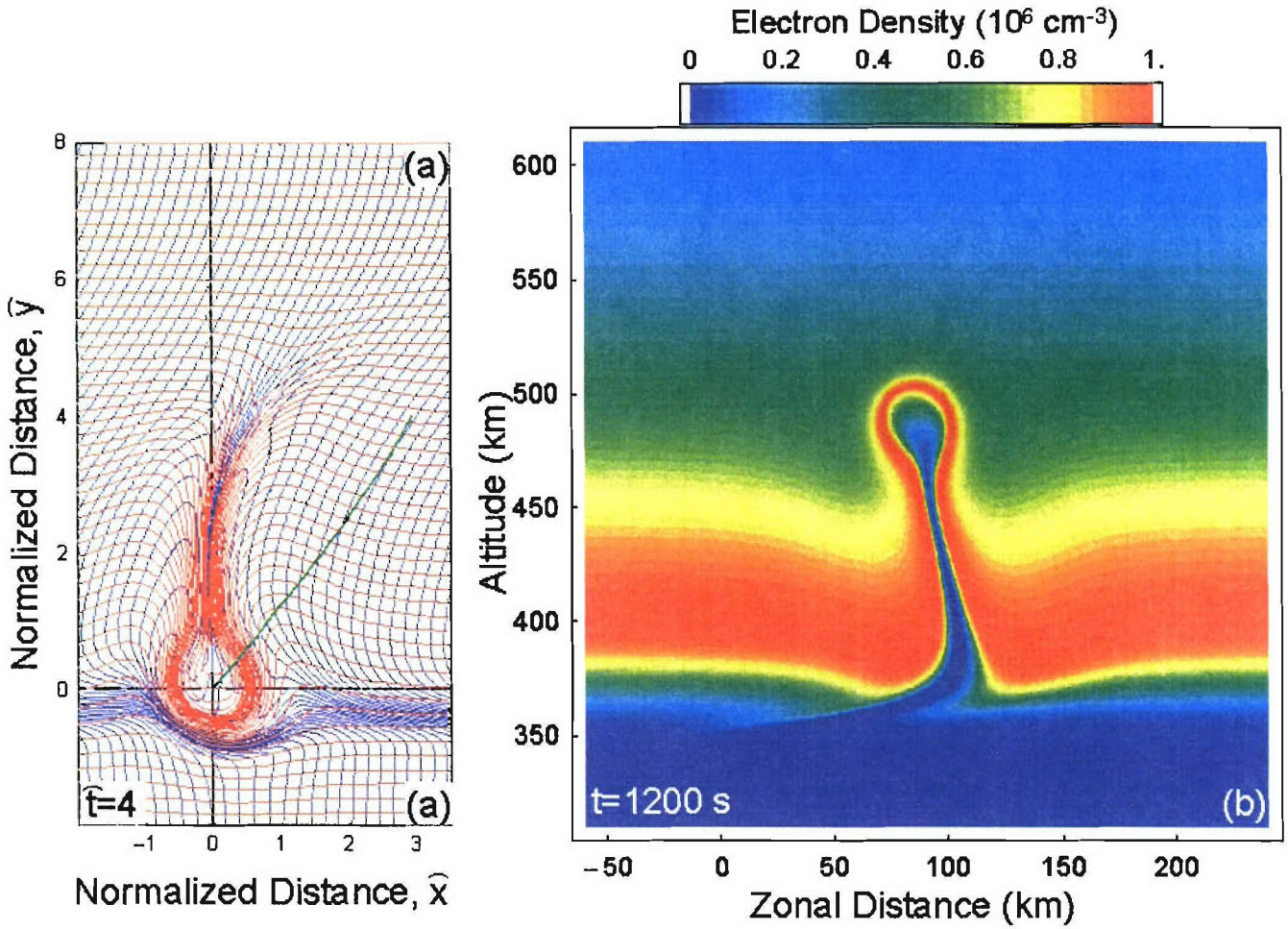$$\hat{x}_0(-t_1) = \hat{x}_1 \text{ and } \hat{y}_0(-t_1) = \hat{y}_1 \tag{69}$$

Figure 18 Computed examples of (a) inverse coordinate map at $\hat{t} = 4$ and (b) corresponding ionospheric bubble densities at t = 1200 seconds for the electric potential moving through a sheared plasma with small internal polarization ($a_y = 0.1$). The parameters for the simulation are identical to those used to generate Figure 11 which can be used for comparison to illustrate the effects of the zonal wind on tilting the bubble.

The inverse coordinate map for the rising bubble the sheared plasma flow is illustrated in Figure 18a in normalized coordinates at the normalized time $\hat{t} = 4$. Using (68), this coordinate map presents the origin of the plasma cells that have been transported to the west by the wind induced horizontal transport and the gravity induced vertical transport. The parameter a_y is set to zero so the horizontal transport by internal polarization of the equatorial bubble is neglected.

When the inverse coordinate map is applied to the background plasma layer, the electron densities are to form the tilted plume structure in Figure 18b. The depletion at the center of the bubble is the result of incompressible convection from the bottom to the topside of the layer. In this model, the reduced density channel extends over 100 km down though the layer to the bottom of the F-region. The absolute spatial dimensions are derived using a scale

length $r_0 = 30$ km and a base height $y_{c0} = 370$ km. As with Figure 16, the time normalization factor is 300 seconds.

VI.   Parameter Normalization in the Analytic Models of the Disturbed Ionosphere

In the simulations of the previous three sections, the electric potential was fixed as it rose through the plasma layer forming bubble structures. The next step in the quasi-analytic modeling is to adjust the model parameters to make the computed electron density consistent with the electric potential. The appropriate values of both parameters (a_x and b) are obtained by comparing the analytic solutions given in (19) with the quasi-analytic solutions obtained by compressing the F-layer coordinates using (42) for an untilted bubble or (67) for a plume with internal polarization and plasma shear flow.

The vertical bubble motion comes from polarization of the horizontal density gradients. The horizontal Pedersen conductivity from (19) though the center of the electric potential is given by

$$\Sigma_p^{(1)}(\hat{x},0) = \exp\left\{\frac{a(1+m)}{A_1}\left[2\tan^{-1}\left(\frac{B_1 - 2|\hat{x}|^b}{A_1}\right) - \text{sign}(a)\,\pi\right]\right\}\frac{C_0\,(1+|\hat{x}|^b)^2}{1-a-B_1|\hat{x}|^b + \hat{x}^{2b}} \qquad (70)$$

where $A_1 = \sqrt{-a[4b + a(b-1)^2]}$ and $B_1 = -a(b-1) - 2$ and $|\hat{x}| = \sqrt{\hat{x}^2}$. Assume that the electron density at the equator is directly proportional to the integrated Pedersen conductivity. In absolute coordinates, the analytic model for the horizontal electron density profile through the center of the bubble is

$$N_e(x_p, y_c(t)) = \exp\left\{\frac{a(1+m)}{A_1}\left[2\tan^{-1}\left(\frac{B_1 - 2|x_p/R_1|^b}{A_1}\right) - \text{sign}(a)\,\pi\right]\right\}\frac{C_1\,(1+|x_p/R_1|^b)^2}{1-a-B_1|x_p/R_1|^b + |x_p/R_1|^{2b}}$$

(71)

where $x_p = x - x_c(t)$ is the horizontal distance relative to the center of the potential function and $\{x_c(t), y_c(t)\}$ is the location of this center. The corresponding electric potential is

$$\Phi(x,y,t) = B_0 \frac{[x - x_c(t)]\,V_{y0}(t) + [y - y_c(t)]\,V_{xR}(y_c(t))}{\left[1 + \left[\left(\frac{x - x_c(t)}{R_1(t)}\right)^2 + \left(\frac{y - y_c(t)}{R_1(t)}\right)^2\right]^{b(t)/2}\right]} \qquad (72)$$

where $a_x(t)$, $b(t)$, $R_1(t)$, and $C_1(t)$ are parameters that will be allowed to vary with time as the bubble evolves. The bubble rise velocity $V_{y0}(t) = \frac{a_x(t)\,E_{Tx}}{B_0}$ and the bubble retardation velocity $V_{xR} = a_y V_{xs}$ have been defined in the previous sections. The electric potential follows a trajectory given by

41

$$\frac{\partial x_c}{\partial t} = V_{x0}(y_c) = (1 - a_y)V_{xS}(y_c)$$

$$\frac{\partial y_c}{\partial t} = V_{y0}(t) = \frac{a_x(t)\,E_{Tx}}{B_0}$$

(73)

With this trajectory, the Lagrangean coordinate map

$$\frac{\partial x(x_0,y_0,t)}{\partial t} = -\frac{1}{B_0}\frac{\partial \Phi(x,y,t)}{\partial y} + V_{xS}(y) \quad \text{and} \quad \frac{\partial y(x_0,y_0,t)}{\partial t} = \frac{1}{B_0}\frac{\partial \Phi(x,y,t)}{\partial x}$$

(74)

is again used to determine the distortion of the plasma layer. The normalization procedure fits the function given by (71) to the densities determined using the Lagrangean transport given by (74) as applied to the stratified plasma profile.

Tests of the normalization procedure has demonstrated that the numerical value for the temporal normalization constant $a_x\,E_{Tx}/(B_0\,r_0)$ is equal to approximately 70% of the calculated growth rate $\gamma = (-E_{Tx}/B_0)/L_N$ of the instability so that the parameter ratio $-r_0/a_x \approx L_N/0.7$. The recommended procedure for providing reasonable models of equatorial bubbles is to first choose a scale length r_0 that matches the dimension of the "seed" needed to produce the bubble. Second, select the potential amplitude using the simple expression $a_x \approx -0.7\,r_0/L_N$ where $L_N = Ne(y)/\dfrac{\partial Ne(y)}{\partial y}$ is the initial scale length of the bottomside of the background ionosphere.

At this point, all the steps outlined in Figure 1b have been completed and the densities for the ionospheric bubble can be computed with relative ease. The only numerical computation is a solution of the ordinary differential equations (74) which are applied to the model of the unperturbed ionosphere. The formulas described here provide the electron densities for propagation of OTH radar signals through the layers to determine the effects of plasma bubbles on the ground clutter signals. The ray trace procedure is described in the next section.

VII.   Ray Trajectories Through the Unstable Ionosphere.

Propagation of HF waves in the ionosphere has been studied for over one-half century. The raytrace code developed to study OTH radar clutter is based on the theory provided by Hazelgrove [1954], Yeh and Liu [1972], Jones and Stephenson [1975], and Budden [1985]. A ray trajectory is characterized by a position vector $\mathbf{r} = (x,y,z)$ and a wave normal direction characterized by the refractive index vector $\mathbf{n} = (n_x, n_y, n_z)$. The wave normal vector $\mathbf{k}$ is related to the refractive index vector by $\mathbf{k} = \mathbf{n}\,\omega/c$ where ω is the wave frequency. If the wave phase ϕ along the ray path starts with a value of zero. At each point on the ray, a

dispersion equation is satisfied with the form $D(x, y, z, n_x, n_y, n_z, \omega) = $ Constant. The canonical equations for the ray path are written as

$$\frac{\partial \mathbf{r}}{\partial P'} = -\frac{\nabla_n D}{\omega \, dD/d\omega} \text{ and } \frac{\partial \mathbf{n}}{\partial P'} = \frac{\nabla_r D}{\omega \, dD/d\omega} \tag{75}$$

where ∇_n and ∇_r are the gradient operator in refractive index and Cartesian space, respectively, $P' = ct$ is the group path and c is the speed of light. The scalar multiplier $dD/d\omega$ is defined as

$$\frac{dD}{d\omega} = \frac{\partial D}{\partial \omega} + \frac{\partial \mathbf{n}}{\partial \omega} \cdot \nabla_n D = \frac{\partial D}{\partial \omega} - \frac{\mathbf{n}}{\omega} \cdot \nabla_n D \tag{76}$$

The phase path front $P = \phi \dfrac{c}{\omega}$ differs from the surface of constant group delay P'. The phase front is computed using

$$\frac{\partial P}{\partial P'} = \mathbf{n} \cdot \frac{\partial \mathbf{r}}{\partial P'} = -\frac{\mathbf{n} \cdot \nabla_n D}{\omega \, dD/d\omega} \tag{77}$$

Two forms of the dispersion equation are used to trace the rays. The Appleton-Hartree dispersion formula is

$$D_{\pm} \equiv n_x^2 + n_y^2 + n_z^2 - 1 + X(1-X)/[1 - X - Y^2 \mathrm{Sin}^2 \psi / 2 \pm R(B_x, B_y, B_z, n_x, n_y, n_z)] = 0 \tag{78}$$

where the radical $R = \sqrt{Y^4 \, \mathrm{Sin}^4 \psi / 4 + Y^2 \, \mathrm{Cos}^2 \psi \, (1-X)^2}$, the plasma frequency squared is $\omega_{pe}^2 = e^2 N_e / (\varepsilon_0 m_e)$, $X = \omega_{pe}^2 / \omega^2$ the plasma frequency normalized by the wave frequency, $Y = eB/(m_e \omega)$ the gyro frequency vector normalized by the wave frequency, and ψ the angle between the wave normal and the magnetic field defined by $\mathbf{n} \cdot \mathbf{B} = n \, B \, \mathrm{Cos} \psi$. The + and − signs in (76) refer to the ordinary and extraordinary modes, respectively. The Booker Quartic dispersion equation is

$$D_q \equiv (1 - X - Y^2) \, n^4 + X \, (\mathbf{n} \cdot \mathbf{Y})^2 \, n^2 + [Y^2(2-X) - 2(1-X)^2] \, n^2 - X \, (\mathbf{n} \cdot \mathbf{Y})^2 + (1-X)[(1-X)^2 - Y^2]$$

(79)

In the plasma where $X \geq 0.1$, dispersion equation (79) is used and if $X < 0.1$, (78) is used to trace the rays. This selection preserves the identity of the mode and allows the rays to change direction at reflection points.

The purpose of the ray tracing is to compute the Doppler shifts of the ground clutter signal in a non-stationary ionosphere. Doppler frequency shift along the ray path is given by

$$\frac{d\Delta\omega}{dP'} = -\frac{1}{c}\frac{\partial D/\partial t}{dD/d\omega} = -\frac{1}{c}\frac{\partial D/\partial N_e}{dD/d\omega}\frac{\partial N_e/\partial t}{}$$ (80)

where it is assumed that all temporal variations in the dispersion are due to fluctuations in the electron density. For this study, the electron density changes are assumed to be the result of transport by electric fields as described in the previous sections. From (1) and (22), the electron density changes due to incompressible transport is given by

$$\frac{\partial N_e}{\partial t} = -\mathbf{v}\cdot\nabla_r N_e = \frac{\nabla_r\Phi\times\mathbf{B}}{B_0^2}\cdot\nabla_r N_e$$ (81)

Combining (80) and (81) yields the equation of the Doppler shift of the received signal in terms of the gradients in the electric potentials and the electron densities in the ionosphere.

$$\frac{d\Delta\omega}{dP'} = \frac{\partial D/\partial N_e}{dD/d\omega}\frac{\mathbf{v}}{c}\cdot\nabla_r N_e = -\frac{\partial D/\partial N_e}{dD/d\omega}\frac{\nabla_r\Phi\times\mathbf{B}}{c B_0^2}\cdot\nabla_r N_e$$ (82)

The Doppler shift for reflection from the ionosphere is referenced to the maximum Doppler shift for specular reflection from a moving mirror given by

$$\Delta\omega_{max} = 2\,\omega\,\frac{v_\parallel}{c}$$ (83)

where $v_\parallel$ is the velocity parallel to the line of sight. A vertical radio ray reflecting the ionosphere at normal incidence will have the Doppler shift of (83). For ground clutter, the maximum Doppler shift is $2\,\Delta\omega_{max}$ because for ground clutter the ray has two reflections from the ionosphere and one from the ground before coming back to the transmission source. A radio wave reflecting with oblique incidence will have a Doppler shift less than $2\,\Delta\omega_{max}$ with a limiting value of zero shift for a horizontally propagating ray with no ionospheric interaction.

The procedure for modeling the OTHR clutter from equatorial bubbles in the ionosphere is to use the quasi-analytic bubble derived in the previous sections to describe the electron density gradients and the electric potential variation. Rays are traced through this ionosphere using (75), (76), (77), and (82). The electron density enters into the equations through (1) the parameter X in the dispersion equations (78) and (79) and (2) the Doppler frequency given by (82). The ray propagates from the ground radar source, is bent by the bottom side ionosphere, and is terminated when the ray path intercepts the ground. The radar signal is scattered by the ground and the ray path follows the identical trajectory back to the radar source. The Doppler at the radar receiver is twice the Doppler at the ground scattering point.

As a test of this ray trace model, the Doppler shifts in the ground clutter will be computed from the F region vertical drifts observed in the quiet time ionosphere. Scherliess and Fejer [1999] use data from the incoherent scatter radar at Jicamarca, Peru and ion drift meter

measurements from atmospheric explorer to derive a global, empirical model of the vertical drifts at the equator. These drifts are in addition to the horizontal plasma drifts illustrated in Figure 14 and the internal plasma drifts associated with the equatorial bubbles. The Scherliess-Fejer model provided the variation in vertical drift illustrated in Figure 19 for calendar days 100 and 240. The largest variation in the vertical drift occurs between 1800 and 2000 local time near dusk. In the spring (Figure 19a) the vertical drift changes from 45.7 m/s upward to 37 m/s downward over the period of two hours. In the summer (Figure 19b) the variations in the vertical drift are smaller.

Figure 19. Local time variation in equatorial vertical drift for quiet time periods. The empirical model drifts represent the longitude near 66° W for (a) solar radio flux of 200 for a day in April and (b) solar radio flux of 116 at the end of August.

Tracing rays though a model ionosphere Figure 13 with the Scherliess-Fejer drift model in (82) gives the predicted Doppler shifts. These will be multiplied by $-\dfrac{c}{2\omega}$, giving the equivalent radial velocity for reflection from a horizontal target. Figure 20a shows the ray paths which are launched with zenith angels ranging from 0 to 80 degrees. The computed Doppler shifts in the received echoes are illustrated in Figure 20b in terms of equivalent radial velocity. The vertical velocities for the ionosphere are taken from the values in Figure 19 at 17:44 local time. One sample of measurements for the radial velocity at a similar local time is shown in Figure 21. The measured Doppler shift of 9.4 m/s is shown by the circle in Figure 20b. The results of this ray trace test show that the ray trace model yields reasonable results for a uniformly rising layer. In practice, the uniform lifting of the ionosphere will produce a shift of all radar signals by a constant amount. This shift will not obscure the radial motion of any targets, since they will share the same apparent Doppler shift.
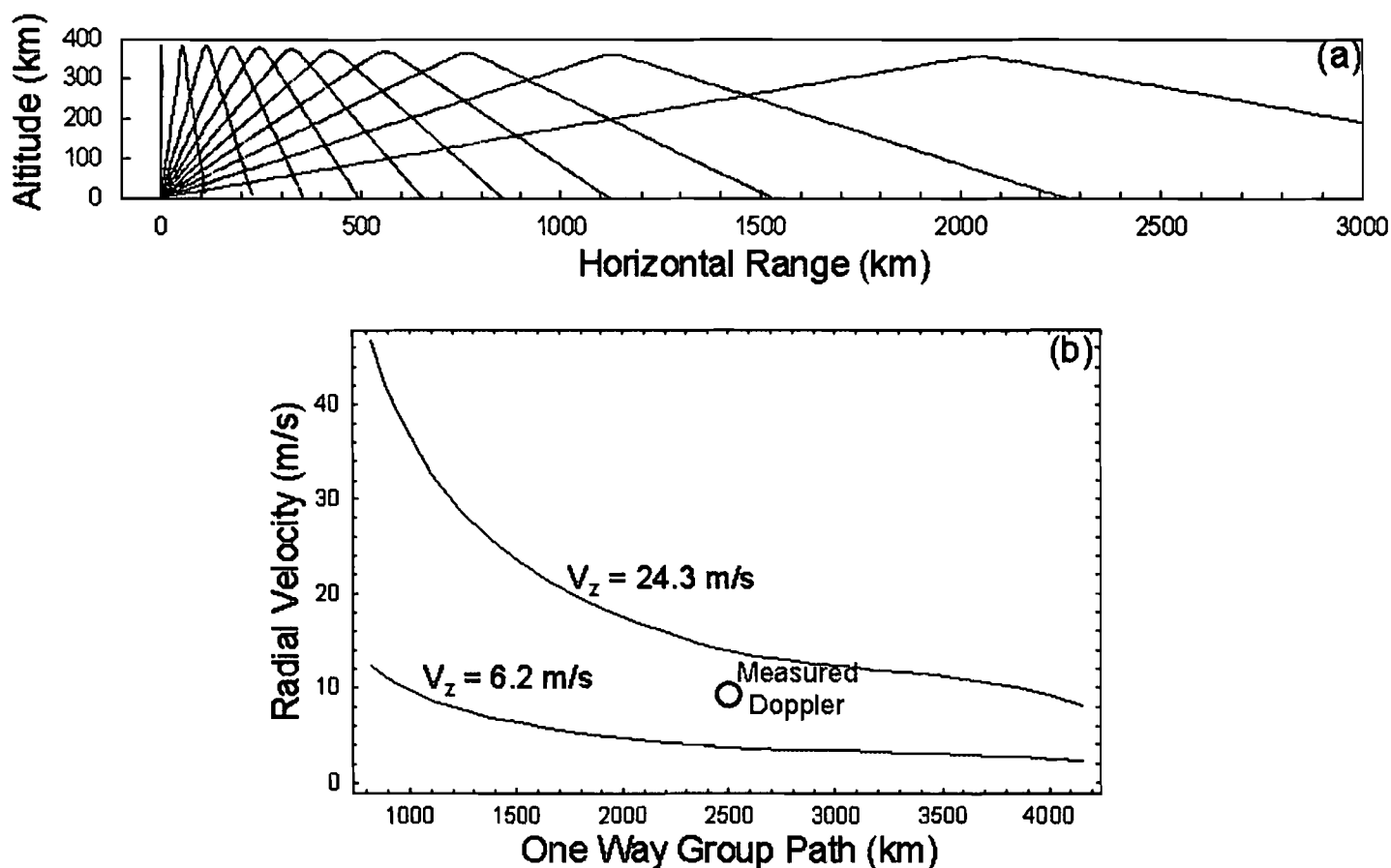

Figure 20. Model calculations of (a) ray trajectories and (b) Doppler shift in ground clutter for two vertical drifts speeds at 17:44 local time. The shortest group paths are for the vertical rays with radial velocities twice the vertical speeds. The measured Doppler shift is illustrated in Figure 21.
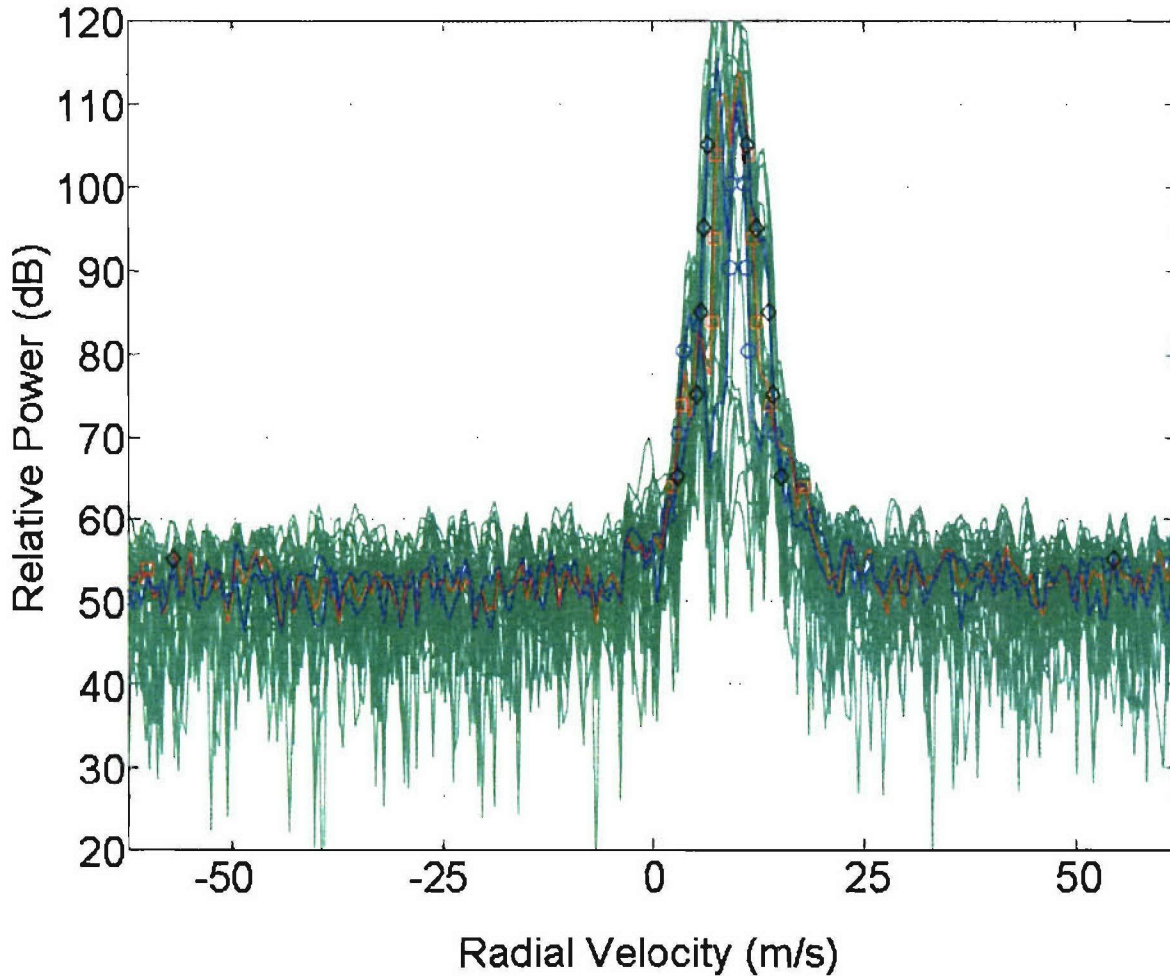
Figure 21. Doppler shift ground clutter on 30 August 2002 at 17:44 Local Time in the Puerto Rican longitudes. The radar frequency is 24.4 MHz and the radar range bin is around 2500 km. The center of the ground clutter peak is found at a radial velocity of 9.4 m/s.

Future research will combine the equatorial model densities illustrated by Figure 18 and the raytrace code used to generate Figure 20. The equatorial bubble densities will be extended along the magnetic meridian using a Dipole field model given by (51). With the dynamics of the equatorial bubbles used in wave propagation, complex Doppler shifts will be generated that provide ground clutter that spreads in frequency or radial velocity. The quasi-analytic tools derived here are uniquely suitable for ray trace studies of ground clutter generation because the rays can be rapidly traced though the density structures and because the Doppler velocities are directly computed by projection of the plasma motion vector along the ray wave normal.

VIII. Summary

Using quasi-analytic solutions of the plasma transport and radio propagation equations, a model was derived to study the effects of ionospheric motion on OTH radar clutter. The quasi-analytic formulation has been derived to imbed ionospheric bubbles in a model background ionosphere. This technique provides a three-dimensional electron density description using the mapping by the electric potential functions of the initial distribution of the ionosphere. This technique has the advantage over a full numerical simulation by providing (1) factors of 10 to 100 enhancements in computational speed, and (2) analytic formulations that are much easier to us for numerical raytracing. The analytic formulation has been benchmarked against full three-dimensional simulations of equatorial bubbles [Zalesak, et al., 1982] currently in use at the Naval Research Laboratory for irregularity simulations. The effects on OTH radar ray-path bending and range Doppler spread for ground clutter have been tested for vertical motion of the equatorial ionosphere. Future studies will investigate for ray paths through the equatorial bubbles that are moving both horizontally and vertically. Finally, possible mitigation strategies for reducing OTH radar clutter effects will be will be tested.

Acknowledgements

Appendices

Appendix A. Numerical Solution of the Potential Equation Using a Direct Solver.

Numerical solutions are required when conditions of simplified geometries or uniform flows yield a complicated, nonlinear partial differential equation for the electric potential. In Cartesian coordinates, the non-separable elliptic equation that describes the electric potential is given by (7) and is repeated in equivalent form here

$$\Sigma_p \frac{\partial^2 \hat{\Phi}}{\partial \hat{x}^2} + \frac{\partial \Sigma_p}{\partial \hat{x}} \frac{\partial \hat{\Phi}}{\partial \hat{x}} + \Sigma_p \frac{\partial^2 \hat{\Phi}}{\partial \hat{y}^2} + \frac{\partial \Sigma_p}{\partial \hat{y}} \frac{\partial \hat{\Phi}}{\partial \hat{y}} = \frac{\partial \Sigma_p}{\partial \hat{x}} \tag{A1}$$

The conductivity function $\Sigma_p(\hat{x}, \hat{y})$ is known and the potential function $\hat{\Phi}(\hat{x}, \hat{y})$ is found as a numerical solution to the equation (A1).

This equation is converted into a set of linear equations using the usual finite difference approximations to the derivatives given by

$$\begin{aligned}
\frac{\partial^2 \hat{\Phi}}{\partial \hat{x}^2} &\rightarrow \frac{\hat{\Phi}_{i+1,j} - 2\hat{\Phi}_{i,j} + \hat{\Phi}_{i-1,j}}{\Delta \hat{x}^2} \\[2mm]
\frac{\partial^2 \hat{\Phi}}{\partial \hat{y}^2} &\rightarrow \frac{\hat{\Phi}_{i,j+1} - 2\hat{\Phi}_{i,j} + \hat{\Phi}_{i,j-1}}{\Delta \hat{y}^2} \\[2mm]
\frac{\partial \hat{\Phi}}{\partial \hat{x}} &\rightarrow \frac{\hat{\Phi}_{i+1,j} - \hat{\Phi}_{i-1,j}}{2\Delta \hat{x}} \\[2mm]
\frac{\partial \hat{\Phi}}{\partial \hat{y}} &\rightarrow \frac{\hat{\Phi}_{i,j+1} - \hat{\Phi}_{i,j-1}}{2\Delta \hat{y}}
\end{aligned} \tag{A2}$$

The Pedersen conductivity is sampled in the uniform solution grid spaced by Δx and Δy to form the array variables $\Sigma_{p_{i,j}}$ with (i=1,2, ..., M) and (j=1, 2, ..., N). To complete the solution, boundary conditions of periodic, fixed/Dirichlet, derivative/Neumann or mixed form are provided.

The unknowns $\hat{\Phi}_{i,j}$ for (i=1,2, ..., M) and (j=1, 2, ..., N) are grouped into linear arrays given by

$$\mathbf{X}_j = [\Phi_{1,j} \ ... \ \Phi_{M,j}] \tag{A3}$$

The resulting linear system can be written as an extended tri-diagonal matrix

$$
\begin{bmatrix}
B_1 & C_1 & 0 & \cdots & 0 & 0 & A_1 \\
A_2 & B_2 & C_2 & \cdots & 0 & 0 & 0 \\
0 & A_3 & B_3 & \cdots & 0 & 0 & 0 \\
\vdots & \vdots & \vdots & \ddots & \vdots & \vdots & \vdots \\
0 & 0 & 0 & \cdots & B_{N-2} & C_{N-2} & 0 \\
0 & 0 & 0 & \cdots & A_{N-1} & B_{N-1} & C_{N-1} \\
D_1 & D_2 & D_3 & \cdots & D_{N-2} & D_{N-1} & D_N
\end{bmatrix}
\begin{bmatrix}
X_1 \\ X_2 \\ X_3 \\ \vdots \\ X_{N-2} \\ X_{N-1} \\ X_N
\end{bmatrix}
=
\begin{bmatrix}
Y_1 \\ Y_2 \\ Y_3 \\ \vdots \\ Y_{N-2} \\ Y_{N-1} \\ Y_N
\end{bmatrix}
\tag{A5}
$$

where the M x M block matrices $A_j, B_j,$ and C_j are functions of the finite difference parameters and the Pedersen conductivity samples $\Sigma_{P_{i,j}}$. The matrices A_1 and D_1 are needed for periodic boundaries in the y-direction. The string of matrices $[D_1, D_2, D_3, ..., D_{N-1}, D_N]$ allow inclusion of an additional condition on the potential such as

$$
\iint \widehat{\Phi}(\widehat{x}, \widehat{y}) \, d\widehat{x} \, d\widehat{y} = 0 \ . \tag{A6}
$$

This condition arises when the addition of a constant to a solution also yields solution. The nonuniqueness occurs if the boundary conditions are completely periodic and/or specified by constant derivatives (i.e., Neumann). With these types of boundary conditions, (A6) prevents the square matrix in (A5) from being singular and a numerical solution can be obtained. Finally, the right side of (A1) and boundary conditions are contained in the linear arrays Y_j .

The algorithm for solving (A5) is a generalization of the Thomas Algorithm for scalar tridiagonal systems [Dahlquist and Bjorck, and Anderson, 1974]. Initialize with new matrix variables

$$
\alpha_1 = B_1^{-1}, \quad S_1 = \alpha_1 \cdot Y_1, \quad a_2 = \alpha_1 \cdot C_1, \quad b_1 = -\alpha_1 \cdot A_1 \tag{A7}
$$

Continue with the equations

$$
a_i = \alpha_{i-1} \cdot C_{i-1}, \quad \alpha_i = [B_i - A_i \cdot a_i]^{-1}, \quad S_i = \alpha_i \cdot [Y_i - A_i S_{i-1}], \quad b_i = -\alpha_i \cdot A_{i-1} \cdot b_{i-1} \tag{A8}
$$

for the index in the range $i = 2, ..., N-1$. The next operations define a new set of variables starting with $S_N' = 0$, $b_N' = I$, where I is the M x M identity matrix, and continue with

$$
S_{N-i}' = S_{N-i} - a_{N-i+1} S_{N-i+1}', \quad b_{N-i}' = b_{N-i} - a_{N-i+1} b_{N-i+1}' \tag{A9}
$$

for the index "i" in the range $i = 1, ..., N-1$. The solution for $j = N$ is given by

$$
X_N = \left[\sum_{i=1}^{N} D_i \cdot b_i' \right]^{-1} \cdot \left[Y_N - \sum_{i=1}^{N} D_i \cdot S_i' \right] . \tag{A10}
$$

The remaining solution vectors are found from

$$\mathbf{X}_i = \mathbf{S}'_i + \mathbf{b}'_i \cdot \mathbf{X}_N \tag{A11}$$

where the index "i" is given by the range $i = 1, ..., N-1$. This algorithm was used to provide the numerical potential solutions illustrated in Figure 5 and the data given in Tables II and III.

Appendix B. Exact Solutions to the Elliptic Potential Equation in Cartesian Coordinates

An analytic solution to the non-separable elliptic equation that relates the Pedersen conductivity to the electric potential in the ionosphere was given by (16). A localized plasma structure may become polarized in a gravitational, neutral wind or electric field flow field. The equation describing this polarization has been given by (4) as

$$\nabla_\perp \cdot (\Sigma_p \nabla_\perp \Phi) = \nabla_\perp \cdot \int [\mathbf{E}_0 + (\mathbf{U} + \frac{\mathbf{g}}{\nu_{in}}) \times \mathbf{B}] \sigma_p dz = \mathbf{E}_T \tag{B1}$$

In Cartesian coordinates, (B1) was written as (7) assuming that only a horizontal equivalent electric field E_{Tx} was present. Here, the total electric field that drives the potential in the general case is assumed to have the from

$$\mathbf{E}_T = E_T (\cos \alpha \ \breve{x} + \sin \alpha \ \breve{y})$$

where $\breve{x}$ and $\breve{y}$ are the unit vectors in the x- and y-directions and α is the angle between the equivalent driving field and the x-axis. In Cartesian coordinates, this equation becomes

$$\frac{\partial^2 \widehat{\Phi}}{\partial \widehat{x}^2} + \frac{\partial \mathrm{Log}(\Sigma_p)}{\partial \widehat{x}} \frac{\partial \widehat{\Phi}}{\partial \widehat{x}} + \frac{\partial^2 \widehat{\Phi}}{\partial \widehat{y}^2} + \frac{\partial \mathrm{Log}(\Sigma_p)}{\partial \widehat{y}} \frac{\partial \widehat{\Phi}}{\partial \widehat{y}}$$
$$= \cos\alpha \frac{\partial \mathrm{Log}(\Sigma_p)}{\partial \widehat{x}} + \sin\alpha \frac{\partial \mathrm{Log}(\Sigma_p)}{\partial \widehat{y}} \tag{B2}$$

where the normalizations $\widehat{\Phi} = \Phi/(r_0 E_T)$, $\widehat{x} = x/r_0$, and $\widehat{y} = y/r_0$ have been used. A general solution can be found using separation of variables with

$$\Phi(\widehat{x}, \widehat{y}) = F(\widehat{x}) G_y(\widehat{y}) \tag{B3}$$

and

$$\Sigma_P(\widehat{x}, \widehat{y}) = H(\widehat{y}) \mathrm{Exp}[\ L_x(\widehat{x})\ ] \tag{B4}$$

With these substitutions into (B2), the solution for the derivative of the L_x is found to be

$$L'_x(\hat{x}) = \frac{[F(\hat{x}) G'_y(\hat{y}) - \sin\alpha] H'(\hat{y}) + H(\hat{y}) [G_y(\hat{y}) F''(\hat{x}) + F(\hat{x}) G''_y(\hat{y})]}{H(\hat{y}) [\cos\alpha - G_y(\hat{y}) F'(\hat{x})]} \qquad (B5)$$

The functions $G_y(\hat{y})$ and $H(\hat{y})$ are chosen so that only a function of $\hat{x}$ remains. Examination of the denominator of (B5) requires that

$$G_y(\hat{y}) = \cos\alpha \qquad (B6)$$

to eliminate one of the functions of $\hat{y}$. With this substitution, (B5) becomes

$$L'_x(\hat{x}) = \frac{\tan\alpha \ H'(\hat{y}) - H(\hat{y}) F''(\hat{x})}{H(\hat{y}) [F'(\hat{x}) - 1]} \qquad (B7)$$

The $\hat{y}$-dependence in $H(\hat{y})$ is eliminated by forcing $H'(y)/H(y) \equiv m$ with the substitution

$$H(\hat{y}) = \text{Exp}(m\,\hat{y}) \qquad (B8)$$

yielding

$$L'_x(\hat{x}) = \frac{m\tan\alpha - F''(\hat{x})}{F'(\hat{x}) - 1}. \qquad (B9)$$

This result (B9) yields the second equation in (13) if $F(\hat{x}) = (a_0 + a_1\hat{x}) G(|\hat{x}|)$ and $\alpha=0$. To summarize, the one dimensional potential function

$$\Phi(\hat{x}, \hat{y}) = F(\hat{x}) \cos\alpha \qquad (B10)$$

is found from is found from (B3) and (B6) for an external electric field $\mathbf{E_T}$ making an angle α with the horizontal axis. The corresponding Pedersen conductivity function is found by substituting (B8) and the integral of (B9) into (B4) with the result

$$\Sigma_P(x,y) = e^{my}\exp\left[\int \frac{m\tan\alpha - F''(x)}{F'(x) - 1}dx\right] \qquad (B11)$$

Rotation of the coordinate axes $(\hat{x}, \hat{y})$ by α so that $\mathbf{E_T}$ is horizontal will yield solutions for obliquely oriented potential functions.

The solution in (B11) is only valid if $\alpha \neq \pi/2$. For the case that $\cos\alpha = 0$, (B5) becomes

$$L'_x(\hat{x}) = -\frac{[F(\hat{x}) G'_y(\hat{y}) - 1] H'(\hat{y}) + H(\hat{y}) [G_y(\hat{y}) F''(\hat{x}) + F(\hat{x}) G''_y(\hat{y})]}{H(\hat{y}) G_y(\hat{y}) F'(\hat{x})} \qquad (B12)$$

52

The only substitutions that eliminate the $\hat{y}$-variations in (B12) are

$$H(\hat{y}) = 1 \quad \text{and} \quad G_y(\hat{y}) = C_1 \exp(-n\hat{y}) + C_2 \exp(n\hat{y}) \tag{B13}$$

where C_1 and C_2 are constants. The resulting log-density function is

$$L_x'(\hat{x}) = -\frac{n^2 F(\hat{x}) + F''(\hat{x})}{F'(\hat{x})}. \tag{B14}$$

To summarize, for the special case that the E_T vector is aligned with the $\hat{y}$-axis ($\alpha = \pi/2$), a potential function of the form

$$\Phi(\hat{x}, \hat{y}) = (C_1 e^{-n\hat{y}} + C_2 e^{n\hat{y}}) F(\hat{x}) \tag{B15}$$

is produced by a Pedersen conductivity variation with the form

$$\Sigma_P(\hat{x}, \hat{y}) = \exp\left[-\int \frac{n^2 F(\hat{x}) + F''(\hat{x})}{F'(\hat{x})} dx \right]. \tag{B16}$$

Rotation of the solutions in (B14) and (B15) by $\pi/2$ yield solutions for a horizontal electric field E_T of the form

$$\Phi(\hat{x}, \hat{y}) = (C_1 e^{-n\hat{x}} + C_2 e^{n\hat{x}}) F(\hat{y}) \quad \text{and} \quad \Sigma_P(\hat{x}, \hat{y}) = \exp\left[-\int \frac{n^2 F(\hat{y}) + F''(\hat{y})}{F'(\hat{y})} dy \right] \tag{B17}$$

These solutions co-exist with the horizontal electric field E_T ($\alpha=0$) solutions of (B10)

$$\Phi(\hat{x}, \hat{y}) = F(\hat{x}) \quad \text{and} \quad \Sigma_P(x, y) = e^{my} \exp\left[-\int \frac{F''(x)}{F'(x) - 1} dx \right] \tag{B18}$$

Thus, with a horizontal external electric field (or equivalently a vertical gravity or neutral wind force), two separate families exact solutions for potentials and densities are available with (B17) and (B18). With rotations the equations (B10) and B(11), a large number of exact oblique solutions can be generated. The example illustrated in Figure 2 is only a small of sample of the analytic results for Cartesian coordinate geometry.

Appendix C. Exact Solutions to the Elliptic Potential Equation in Cylindrical Coordinates

A second general solution to the potential equation can be derived by using cylindrical coordinates by selecting either radial or axial symmetric for the function representations. As defined previously in (4) and (B1), the elliptic equation describing the relation between the Pedersen conductivity (Σ_P) and the electric potential (Φ) is given as

$$\nabla_\perp \cdot (\Sigma_p \nabla_\perp \Phi) = \nabla_\perp \cdot \int [E_0 + (U + \frac{g}{v_{in}}) \times B] \sigma_p dz = E_T \tag{C1}$$

Assume that ambient forces yield motion in the y-direction by an equivalent electric field E_{Tx} in the x-direction given by

$$E_{Tx} \equiv [E_{0x} + (U_y - \frac{g_0}{v_{in}})B_0] \tag{C2}$$

The cylindrical (r, θ, z) coordinates are related to Cartesian coordinates by

$$x = r \, Cos\theta$$
$$y = r \, Sin\theta \tag{C3}$$
$$z = z$$

and the unit vector in the x- direction is

$$\breve{x} = \cos\theta \, \breve{r} - \sin\theta \, \breve{\theta} \tag{C4}$$

In the cylindrical coordinate system, the potential equation becomes

$$\Sigma_p (r^2 \frac{\partial^2 \Phi}{\partial r^2} + r \frac{\partial \Phi}{\partial r} + \frac{\partial^2 \Phi}{\partial \theta^2}) + r^2 \frac{\partial \Sigma_p}{\partial r} \frac{\partial \Phi}{\partial r} + \frac{\partial \Sigma_p}{\partial \theta} \frac{\partial \Phi}{\partial \theta} = E_{Tx} (r^2 \, Cos\theta \frac{\partial \Sigma_p}{\partial r} - r \, Sin\theta \frac{\partial \Sigma_p}{\partial \theta}) \tag{C4}$$

After normalization this equation is written as

$$\begin{aligned} \hat{r}^2 \frac{\partial^2 \hat{\Phi}}{\partial \hat{r}^2} + \hat{r} \frac{\partial \hat{\Phi}}{\partial \hat{r}} + \frac{\partial^2 \hat{\Phi}}{\partial \theta^2} + \hat{r}^2 \frac{\partial \log(\Sigma_p)}{\partial \hat{r}} \frac{\partial \hat{\Phi}}{\partial \hat{r}} + \frac{\partial \log(\Sigma_p)}{\partial \theta} \frac{\partial \hat{\Phi}}{\partial \theta} \\ = \hat{r}^2 \cos\theta \frac{\partial \log[\Sigma_p]}{\partial \hat{r}} - \hat{r} \sin\theta \frac{\partial \log[\Sigma_p]}{\partial \theta} \end{aligned} \tag{C5}$$

where the previously defined normalizations $\hat{\Phi} = \Phi / E_{Tx}$ and $\hat{r} = r/r_0$ have been used.

To obtain one class of radial-dependent solutions, apply separation of variables with the substitutions

$$\hat{\Phi}(\hat{r}, \theta) = F(\theta) G_r(\hat{r}) \tag{C6}$$

and

$$\Sigma_P(\hat{r}, \theta) = H(\theta) \exp[L_r(\hat{r})] \tag{C7}$$

Then, solve for $L_r(\hat{r})$ in terms of functions that only depend on r . With the substitution of (C6) and (C7) in to (C5), the solution for the first derivative of $L_r(\hat{r})$ is

$$L_r'(\hat{r}) = -\frac{[\hat{r}\sin\theta + G_r(\hat{r})F'(\theta)]H'(\theta) + G_r(\hat{r})H(\theta)F''(\theta) + \hat{r}\,F(\theta)H(\theta)[\,G_r'(\hat{r}) + \hat{r}\,G_r''(\hat{r})]}{\hat{r}^2 H(\theta)[\cos\theta - F(\theta)\,G_r'(\hat{r})]} \tag{C8}$$

The first step in elimination of the θ dependences on the right side of (C8) is to let $F(\theta) = \cos\theta$ with the result

$$L_r'(\hat{r}) = -\frac{G_r(\hat{r})[1 + \tan\theta\,H'(\theta)/H(\theta)] - \hat{r}\,[\tan\theta\,H'(\theta)/H(\theta) + G_r'(\hat{r}) + \hat{r}\,G_r''(\hat{r})]}{\hat{r}^2\,[\,G_r'(\hat{r}) - 1]} \tag{C9}$$

Next, the θ dependent relation $\tan\theta\,H'(\theta)/H(\theta)$ in (C9) is set equal to a constant "m". The solution of $\tan\theta\,H'(\theta)/H(\theta) \equiv m$ is $H(\theta) = C_1\sin^m\theta$ where C_1 is a constant. With these substitutions, (C6) and (C7) become

$$\Phi(\hat{r}, \theta) = \cos\theta\,G_r(\hat{r}) \text{ and } \Sigma_P(\hat{r}, \theta) = \sin^m\theta\,\exp[L_P(\hat{r})] \ . \tag{C10}$$

and (C8) is reduced to

$$L_r'(\hat{r}) = -\frac{\hat{r}\,m + (1 + m)G_r(\hat{r}) - \hat{r}\,G_r'(\hat{r}) - \hat{r}^2\,G_r''(\hat{r})}{\hat{r}^2[1 + G_r'(\hat{r})]} \tag{C11}$$

where the right side is only a function of $\hat{r}$. After integration and substitution into (C7), the Pedersen conductivity is found to be

$$\Sigma_P(\hat{r}, \theta) = \sin^m\theta\,\exp\{\int -\frac{\hat{r}\,m + (1 + m)G_r(\hat{r}) - \hat{r}\,G_r'(\hat{r}) - \hat{r}^2\,G_r''(\hat{r})}{\hat{r}^2[1 + G_r'(\hat{r})]}\,d\hat{r}\} \tag{C12}$$

Equation (C12) identical to (16) if $G_r(\hat{r}) = \hat{r}\,G(\hat{r})$ and $L_P'(\hat{r}) = L_r'(\hat{r}) - m/\hat{r}$.

To obtain a complementary set of angular-dependent solutions, use separation of variables with the functions

$$\hat{\Phi}(\hat{r}, \theta) = F_\theta(\theta)\,G(\hat{r}) \tag{C13}$$

and

$$\Sigma_P(r, \theta) = H(\theta) \exp[L_\theta(\theta)] \tag{C14}$$

and solve for $L_\theta(\theta)$ in terms of functions that only depend on θ. With (C13) and (C14), (C5) is rewritten as

$$L'_\theta(\theta) = \frac{r^2 \cos\theta\, H'(\hat{r}) + G(\hat{r})\, H(\hat{r})\, F''_\theta(\theta\theta + \hat{r}\, F_\theta(\theta\theta)\, G'(\hat{r})[H(\hat{r}) + \hat{r}\, H'(\hat{r})] + \hat{r}\, H(\hat{r})\, G'_r(\hat{r})\}}{H(\hat{r})[\hat{r}\sin\theta - G(\hat{r})\, F'_\theta(\theta)]}$$
(C15)

The first step for elimination of functions of r from (C15) is to let $G(\hat{r}) = \hat{r}$ so (C15) simplifies to

$$L'_\theta(\theta) = \frac{\hat{r}\cos\theta\, H'(\hat{r})/\, H(\hat{r}) + F''_\theta(\theta) + F_\theta(\theta)[1 + r\, H'(\hat{r})/\, H(\hat{r})]\}}{\sin\theta - F'_\theta(\theta)]} \tag{C16}$$

The r dependence is removed from (C16) by letting $H(\hat{r}) = \hat{r}^m$ so $\hat{r}\, H'(\hat{r})/H(\hat{r}) \equiv m$ where "m" is a constant. With this substitution, (C16) is further reduced to

$$L'_\theta(\theta) = \frac{m\cos\theta + F''_\theta(\theta) + F_\theta(\theta)(1 + m)\}}{\sin\theta - F'_\theta(\theta)}$$

In summary, if the potential has the form

$$\Phi(\hat{r}, \theta) = \hat{r}\, F_\theta(\theta) \tag{C17}$$

and the Pedersen conductivity has the form

$$\Sigma_P(\hat{r}, \theta) = \hat{r}^m \exp[L_\theta(\theta)]. \tag{C18}$$

This is written out as the integral equation

$$\Sigma_P(\hat{r}, \theta) = \hat{r}^m \exp\{ \int \frac{m\cos\theta + (1 + m)F_\theta(\theta) + F''_\theta(\theta)}{\sin\theta - F'_\theta(\theta)} d\theta \} \tag{C19}$$

This solution is given for completeness. There have been no useful applications of (C19) to the ionosphere because the initial potential grows with radius and the radial electric field extends indefinitely.

References

Basu, B., On the linear theory of equatorial plasma instability: comparison of different descriptions, **J. Geophys. Res., 107**, doi:10.1029/2001JA000317, 2002.

Bernhardt, P.A. and J.U. Brackbill, "Solution of Elliptic Equations Using Fast Poisson Solvers," **J. Comp. Phys.**, 53, 382, 1984.

Bernhardt, P.A., Cross-B convection of artificial created, negative-ion clouds and plasma depressions: low-speed flows, **J. Geophys. Res., 93**, 8696-8704, 1988.

Bernhardt, P.A., Eye on the Ionosphere: Ionospheric Profiling by GPS Receiver Occultations, Taking Advantage of Existing Earth-Based Infrastructure, **GPS Solutions**, 9, 174-177, 2005.

Budden, K.G., **The Propagation of Radio Waves**, Cambridge University Press, Cambridge, 1985.

Chen, K. Y., H. C. Yeh, S. Y. Su, and C. H. Liu, Anatomy of plasma structures in an Equatorial spread-F event, **Geophys. Res. Lett., 28**, 3107, 2001.

Huang, C. S., M. C. Kelley, and D. L. Hysell, Nonlinear Rayleigh Taylor instabilities, atmospheric gravity waves, and equatorial spread-F, **J. Geophys. Res., 98**, 15,631, 1993.

Huang, C. Y., W. J. Burke, J. S. Machuzak, L. C. Gentile, and P. J. Sultan, DMSP observations of equatorial plasma bubbles in the topside ionosphere near solar maximum, **J. Geophys. Res., 106**, 8131, 2001.

Huba, J. D., G. Joyce, and J. A. Fedder, Sami2 is another model of the ionosphere (SAMI2): A new low-latitude ionosphere model, **J. Geophys. Res., 105**, 23,035, 2000.

Hysell, D. L., C. E. Seyler, and M. C. Kelley, Steepened structures in equatorial spread-F: Theory, **J. Geophys. Res., 99**, 8841, 1994.

Kelley, M. C., J. J. Makela, B. Ledvina, and P. M. Kintner, Observations of equatorial spread-F from Haleakala, Hawaii, **J. Geophys. Res., 29**, doi:10.1029/2002GL015509, 2002.

Keskinen, M. J., S. L. Ossakow, S. Basu, and P. Sultan, Magnetic flux tube integrated evolution of equatorial ionospheric plasma bubbles, **J. Geophys. Res., 103**, 3957, 1998.

Keskinen, M. J., S. L. Ossakow, and P. K. Chaturvedi, Preliminary report of numerical simulations of intermediate wavelength collisional Rayleigh Taylor instability in equatorial spread-F, **J. Geophys. Res., 85**, 1775, 1980.

Kil, H., and R. A. Heelis, Global distribution of density irregularities in the equatorial ionosphere, **J. Geophys. Res., 103**, 407, 1998.

Otsuka, Y., K. Shiokawa, T. Ogawa, and P. Wilkinson, Geomagnetic conjugate observations of equatorial airglow depletions, **Geophys. Res. Lett, 29**, doi:10.1029/2002GL015347, 2002.

Ott, E., Theory of Rayleigh -Taylor bubbles in the equatorial ionosphere, J. Geophys. Res., 83, 2,066, 1978.

Richtmyer, R.D., and K.W. Morton, **Difference Methods for Initial-Value Problems**, Interscience, New York, 1967.

Sahai, Y., P. R. Fagundes, and J. A. Bittencourt, Transequatorial F-region ionospheric plasma bubbles: Solar cycle effects, **J. Atmos. Terr. Phys., 62**, 1377, 2000.

Scannapieco, A. J., and S. L. Ossakow, Nonlinear spread-F, **Geophys. Res. Lett., 3,** 451, 1976.

Scherliess, L., and B. G. Fejer, Radar and satellite global equatorial F region vertical drift model, **J. Geophys. Res., 104,** 6829, 1999.

Sekar, R., R. Suhasini, and R. Ragvaharo, Evolution of plasma bubbles in the equatorial F-region with different seeding conditions, **Geophys. Res. Lett., 22,** 885, 1995.

Stephan, A.W.,M. Colerico, M. Mendillo, B.W. Reinisch, and D. Anderson, Suppression of equatorial spread-F by sporadic E, **J. Geophys. Res., 107,** doi:10.1029/2001JA000162, 2002.

Sultan, P. J., Linear theory and modeling of the Rayleigh -Taylor instability leading to the occurrence of equatorial spread F, J. Geophys. Res., 101, 26,875, 1996.

Weber, E. J., et al., Equatorial plasma depletion precursor signatures and onset observed south of the magnetic equator, **J. Geophys. Res., 101,** 26,829, 1996.

Yeh, H. C., S. Y. Su, and R. A. Heelis, Storm time plasma irregularities in the pre-dawn hours observed by the low latitude ROCSAT-1 satellite at 600 km altitude, **J. Geophys. Res., 28,** 685, 2001.

Yeh, K.C., and C.H. Liu, **Theory of Ionospheric Waves,** Academic Press, New York, 1972.

Zalesak, S. T., Fully multidimensional flux corrected transport algorithms for fluids, **J. Comput. Phys., 31,** 355, 1979.

Zalesak, S.T., S.L. Ossakow, P.K. Chaturvedi, Non-linear equatorial spread-F – The effect of neutral winds and background Pedersen conductivity, **J. Geophys. Res., 87,** 151-166, 1982.